AUTOMATIC INITIALIZATION OF ACTIVE CONTOURS FOR SEGMENTATION OF ULTRASOUND IMAGES OF BREAST CANCER
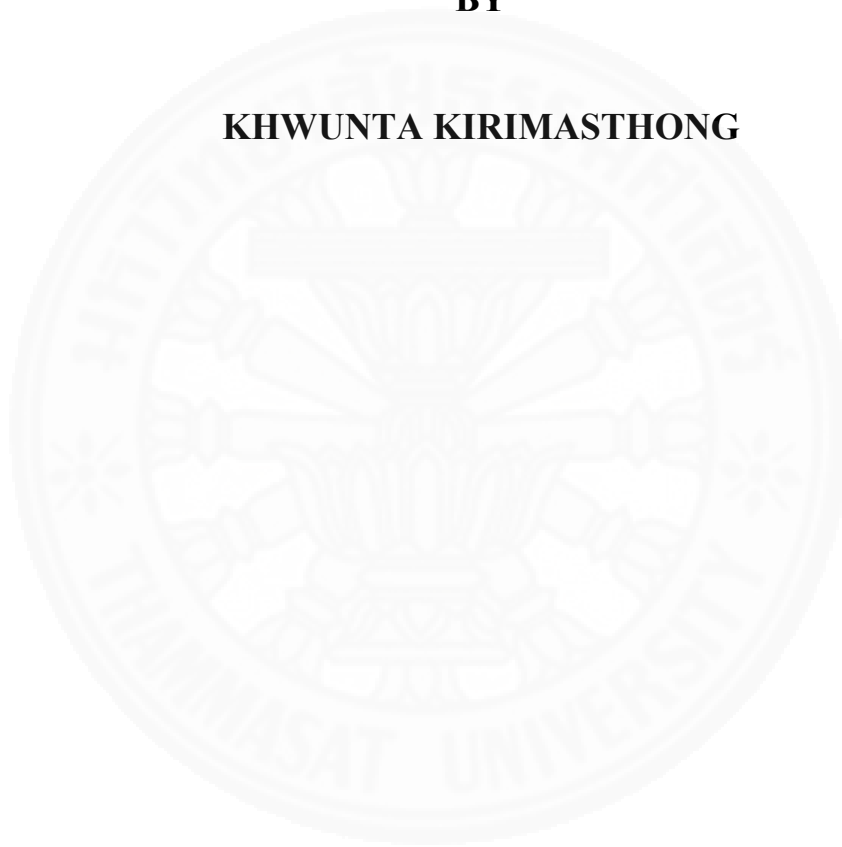
BY

KHWUNTA KIRIMASTHONG

A DISSERTATION SUBMITTED IN PARTIAL FULFILLMENT OF THE REQUIREMENTS FOR THE DEGREE OF DOCTOR OF PHILOSOPHY (ENGINEERING AND TECHNOLOGY) SIRINDHORN INTERNATIONAL INSTITUTE OF TECHNOLOGY THAMMASAT UNIVERSITY ACADEMIC YEAR 2017

AUTOMATIC INITIALIZATION OF ACTIVE CONTOURS FOR SEGMENTATION OF ULTRASOUND IMAGES OF BREAST CANCER

BY

KHWUNTA KIRIMASTHONG

A DISSERTATION SUBMITTED IN PARTIAL FULFILLMENT OF THE REQUIREMENTS FOR THE DEGREE OF DOCTOR OF PHILOSOPHY (ENGINEERING AND TECHNOLOGY) SIRINDHORN INTERNATIONAL INSTITUTE OF TECHNOLOGY THAMMASAT UNIVERSITY ACADEMIC YEAR 2017

AUTOMATIC INITIALIZATION OF ACTIVE CONTOURS FOR
SEGMENTATION OF ULTRASOUND IMAGES OF BREAST CANCER

A Dissertation Presented

By

KHWUNTA KIRIMASTHONG

Submitted to

Sirindhorn International Institute of Technology

Thammasat University

In partial fulfillment of the requirements for the degree of

DOCTOR OF PHILOSOPHY (ENGINEERING AND TECHNOLOGY)

Approved as to style and content by
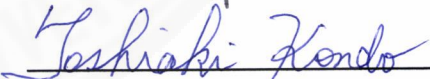
Advisor and Chairperson of Thesis Committee _____

(Prof. Dr. Stanislav S. Makhanov)

Co-Advisor _____

(Asst. Prof. Dr. Annupan Rodtook)

Committee Member and
Chairperson of Examination Committee _____

(Assoc. Prof. Dr. Toshiaki Kondo)

Committee Member _____

(Assoc. Prof. Dr. Bunyarit Uyyanonvara)

Committee Member _____

(Assoc. Prof. Dr. Matthew Dailey)

External Examiner: Prof. Dr. Reyer Zwiggelaar

OCTOBER 2017

i

Abstract

AUTOMATIC INITIALIZATION OF ACTIVE CONTOURS FOR SEGMENTATION OF ULTRASOUND IMAGES OF BREAST CANCER

by

KHWUNTA KIRIMASTHONG

Bachelor of Science (Computer Science, 2nd Class Honors), Chiang Mai University, 2004

Master of Science (Computer Science), Chiang Mai University, 2007

Doctor of Philosophy (Engineering and Technology), Sirindhorn International Institute of Technology, Thammasat University, 2017

Segmentation of ultrasound (US) image of breast cancer is one of the most challenging problems of modern medical image processing. A number of popular codes for US image segmentation are based on the active contours (snakes) and on a variety of modifications of gradient vector flow (GVF). The snakes have been used to locate objects in various medical images. The main difficulty in applying the methods is initialization. The GVF snakes produce inaccurate results if the initial contours (seeds) are initialized inappropriately i.e. far from the real boundaries or/and close to the false boundaries (noise and artifacts). Therefore, the subject of dissertation is a novel method for automatic initialization of GVF-type active contours. The first proposed method is based on phase portrait analysis (PPA) of the underlying vector field and a sequential initialization of multiple trial snakes (TS). The PPA makes it possible to exclude the noise and artifacts and properly initialize the multiple snakes. In turn, the TS method allows us to differentiate between the seeds initialized inside or outside the desired object. The second proposed method is based on exploding seeds (ES) or walking particles. At the first step, the algorithm locates the seeds at converging and diverging configurations of the vector field. At the second step, the seeds "explode", generating a set of walking particles designed to differentiate

between the seeds generated inside and outside the object. The TS and ES outperform five state-of-the-art initialization algorithms.

Keywords: image segmentation, medical images, ultrasound, active contours, automatic initialization, gradient vector fields, exploding seeds, phase portrait analysis.

Acknowledgement

Table of Contents

vii

List of Tables

List of Figures

Chapter 1
Introduction

The computer aided systems for the medical image segmentation help the radiologists or physicians to pre-locate the features of interest, increase the diagnosis accuracy and reduce the image reading time [1]. Presently, mathematics, statistics and computer science methods are applied to analyze the medical images. Many types of imaging techniques such as Mammography, Computed Tomography, Magnetic Resonance Imaging , Ultrasound (US) imaging [2], Doppler and elasticity imaging [3-6] are used for scanning of breast cancer (see Figure 1.1).

Breast cancer is the most common cancer worldwide for women [1]. In particular in Thailand, it is reported in the hospital-based cancer registry annual report 2015 of the National Cancer Institute [6]. Early detection increases the patient's survival rate and offers more treatment options [1]. The mammography is an effective tool for early screening of breast cancer. However, it still has some limitation such as low sensitivity (non-cancer lesions can be misinterpreted as a cancer, while cancers may be missed [1]). Due to some restrictions of mammogram imaging, the US and MRI screening are often suggested for further analysis. Currently, the most effective tool which supplements the mammogram screening is the ultrasound [1]. The ultrasound imaging or sonography is a technique that utilizes the high-recurrence sound wave to create dynamic virtual images of organs, tissues, or blood streams [2]. However, the US images are operator-dependent and still require expert radiologists for interpretation [1]. Therefore, the computerized segmentation systems may increase the accuracy of breast cancer detection.

One of the most popular techniques for extraction of complex objects from digital image is active contours or snakes originally proposed by Kass and colleagues [8]. The performance of the classical snakes can be improved by using higher-order parametric models proposed by Rochery et al. [9]. Further, the accuracy can be enhanced by improving the external force field. Xu and Prince propose the gradient

1

vector flow (GVF) [10] to increases the capture range of the snake and the generalized gradient vector flow (GGVF) [11] which introduces weighting functions and non-linear diffusion coefficient.

The computational time and the accuracy of the snakes critically depend on the initial contours (seeds). Noise and small objects may attract the snake to a local energy minimum, which does not correspond to the actual boundary. Therefore, to reach the boundary of desired object, the initial contour should be initialized close to the object boundary. The problem can be partially solved by initializing multiple snakes, which can split, merge, and collapse (disappear). Moreover, the higher-order active contours (quadratic snakes) proposed by Rochery et al. [9] are able to "see" each other, so that they do not intersect if not required. However, such strategies still require proper initialization.

Numerous research papers apply the active contours and a variety of their modifications to extract the object of interest from medical images. However, as mentioned above, the snakes strongly depend on the initialization. If the seeds of initial snakes are initialized improperly i.e. far from the real boundaries and/or close to the false boundaries, the snakes may get attracted to them and produce inaccurate segmentation results. Unfortunately, up to now only a few papers deal with the snake initialization. The majority of the existing models offer the user to define the initial contour manually [10-13]. The competing level-set method [14] also requires a manually initialized initial surface. The quasi-automatic initialization [15] defines an initial skeleton snake generated around the centers of strong and weak divergence of the gradient vector flow. Besides, it still requires one manually selected point inside the object. The Poisson inverse gradient flow is combined with Canny edge detection and obtained by a genetic algorithm [16]. However, the method is sensitive to the artifacts and noise. As far as the US images are concerned, the majority of the initialization methods are based on the analysis of the gray levels and textures, to locate the most probable seed points [17-19]. However, all the above methods depend on the particular features of the image and may not work if a strong noise is present.

2

Therefore, this dissertation offers two algorithms for automatic initialization which combine the multiple competing active contours [16] and the idea of vector field analysis [20].

The first proposed method called the Trial Snake (TS) relies on the idea of vector field analysis using PPA [20] and multiple GVF-type snakes [16]. Note that PPA has been used in a variety of image processing applications, e.g. [21-27]. However, the PPA in the framework of initialization algorithms has been actually overlooked. The PPA makes it possible to exclude the noise and artifacts and properly initialize the seeds of multiple snakes. In turn, the trial snakes allow us to differentiate between the seeds initialized inside or outside the desired object. If the trial snakes grow and reach the image border, the seeds are classified as external, otherwise they are considered to be the internal candidate seeds.

The second proposed method called the Exploding Seeds (ES) is based on walking particles. At the first step, the algorithm locates the seeds at converging and diverging configurations of the vector field obtained from the PPA. At the second step, the seeds "explode", generating a set of walking particles designed to differentiate between the seeds generated inside and outside the object. If the majority of the particles originated from the particular seed reach the image border, they are classifies as the external seeds, otherwise, they are the candidate internal seeds.

The numerical experiments show the advantages of the TS and ES with the reference to five state-of-the-art initializations. We also show that the active parametric contours endowed with the proposed initialization outperform the level set method [28] and Fuzzy C–Mean clustering [29].

This dissertation consists of five chapters. Chapter 1 is an introduction, problem statement, motivation, objective and outline of the dissertation. Chapter 2 is a literature review. Chapter 3 presents the Trial Snakes Model. Chapter 4 presents the Exploding Seeds Model. Chapter 5 deals with conclusions and future work.
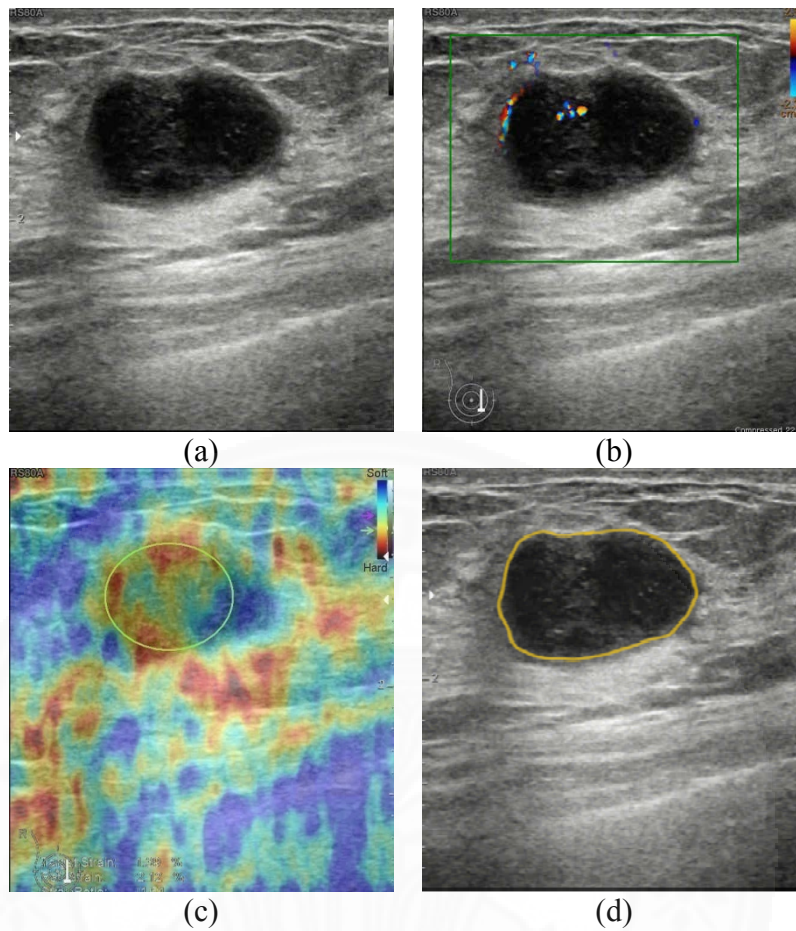
Figure 1.1 Images of malignant solid mass from [7], (a) Ultrasound image, (b) Doppler image, (c) Elastography image, (d) Ground truth image hand-drawn by a radiologist.

4

Chapter 2
Literature Review

The chapter presents a literature review which includes snake-based segmentation for medical image processing, GVF–type active contours, phase portrait analysis (PPA), charged particles for edge detection and current state of the art of snake initialization methods.

2.1 Generalized Gradient Vector Flow Active Contours

An active contour or snake is a parametric curve $X(s)=(x(s),y(s)), s \in [0,1]$ involving inside the image domain (grows or contracts) to attach itself to the boundary of the object of interest. The evolution of the snake is simulated by Euler equations, corresponding to minimization of a certain energy functional [8]. The equation are given by

$$a\frac{d^2 X}{ds^2}+b\frac{d^4 X}{ds^4}+\nabla E_{ext}=0,\tag{2.1}$$

where a and b are weighting parameters to control the snake's tension and rigidity and ∇E_{ext} is the GVF type gradient vector flow. One of the most popular is the GGVF [11], obtained by solving the following system of partial derivative equations

$$\frac{\partial V}{\partial t}-g\left(|\nabla f|\right)\nabla^2 V-h\left(|\nabla f|\right)(\nabla f - V)=0,\tag{2.2}$$

where f is the image edge map, $g(|\nabla f|)=e^{-(|\nabla f|/K)}$, $h(|\nabla f|)=1-g(|\nabla f|)$, and K is a calibration parameter. Among numerous extensions of the GGVF type gradient vector flow idea are Normal Gradient Vector Flow [30], Infinity Laplacian [31], Harmonic Gradient Vector Flow [32], Convolution Vector Flow [33], Dynamic Directional Gradient Vector Flow [34], Adaptive Diffusion Flow [35], and Multi Feature Gradient Vector Flow [36].

5

2.2 Phase Portrait Analysis
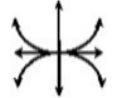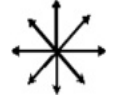
The idea to use the PPA for oriented patterns in image processing has been used in fingerprint identification [23, 27], texture analysis [26], and satellite imagery [21, 22]. PPA techniques have been also applied to detect architectural distortions in mammogram breast images [37]. As far as the initialization of active contours is concerned, He et al. [38] use the PPA and a Boolean classifier to initialize snakes at the centers of divergence. However, the method can not differentiate the internal and external seeds.

PPA is based on the analysis of the vector flow V assumed to change linearly in the neighborhood of the critical point $p = (x, y)$ as follows, $V = Ap$, where A is the corresponding matrix. The matrix is approximated by the least square method applied to V in the moving window centered at p. The flow is characterized by the eigenvalues of A (see Table 2.1), where λ_1, λ_2 are the eigenvalues, $R_i = \operatorname{Re} \lambda_i$, $I_i = \operatorname{Im} \lambda_i$, and $i = 1, 2$ [39, 40]. The phase portrait patterns are illustrated in Table 2.1. The following classifier has been proposed [40]

$$C_{i,j}(W) = \begin{cases} \text{boundary}, & \dfrac{\min(|\lambda_1|, |\lambda_2|)}{\max(|\lambda_1|, |\lambda_2|)} \leq \Delta_1, \ \ |\lambda_1| > \Delta_2 \ \text{or} \ |\lambda_2| > \Delta_2, \\[2mm] \text{noise}, & \dfrac{\min(|\lambda_1|, |\lambda_2|)}{\max(|\lambda_1|, |\lambda_2|)} > \Delta_1, \ \ |\lambda_1| > \Delta_2 \ \text{or} \ |\lambda_2| > \Delta_2, \\[2mm] \text{regular point}, & |\lambda_1| \leq \Delta_2 \ \text{or} \ |\lambda_2| \leq \Delta_2, \end{cases} \quad , \qquad (2.3)$$

where W is the window around the pixel i, j, and Δ_1, Δ_2 are the thresholds evaluated by training.

Table 2.1 Phase portrait analysis of 2D critical points

Pattern	Eigenvalues		Illustration
Repelling Focus	$R_1 = R_2 > 0$	$I_1 = -I_2 \neq 0$	
Attracting Focus	$R_1 = R_2 < 0$	$I_1 = -I_2 \neq 0$	
Saddle Point	$R_1 > 0, R_2 < 0$	$I_1 = I_2 = 0$	
Repelling Node	$R_1 \neq R_2 > 0$	$I_1 = I_2 = 0$	
Attracting Node	$R_1 \neq R_2 < 0$	$I_1 = I_2 = 0$	
Center	$R_1 = R_2 = 0$	$I_1 = -I_2 \neq 0$	
Repelling Star	$R_1 = R_2 > 0$	$I_1 = I_2 = 0$	
Attracting Star	$R_1 = R_2 < 0$	$I_1 = I_2 = 0$	
Pure Shear	$R_1 = R_2 = 0$	$I_1 = I_2 = 0$	
Node-Saddle1: Repelling	$R_1 > 0, R_2 = 0$	$I_1 = I_2 = 0$	
Node-Saddle 2: Attracting	$R_1 < 0, R_2 = 0$	$I_1 = I_2 = 0$	

7

2.3 Charged Particle Method for Edge Detection

The charged particle method for edge detection was introduced by Jalba and colleagues [41]. This method is motivated by classical electrodynamics and is based on a simulation of the moving charged particles in an electrostatic field. The charged particles are attracted by an electric field acting towards the boundary of the object. The particles' sources are computed based on the edge map of image. The idea was further developed in [42, 43].

2.4 Snake-based Segmentation for Medical Image Processing

Many segmentation methods have been developed for US images of breast cancer. Numerous reviews (e.g. [44, 45]) present methods to treat segmentation of medical images as a general image processing problem while others use a priori information relevant to the specific type of the images. Conventional segmentation methods include thresholding [46-50], neural networks [51-58], mode-based methods (such as expectation–maximization) [59, 60], clustering [61, 62], region growing [63], deformable active contours (snakes) [17, 46, 64-67] and level set methods [14]. The segmentation is usually followed by feature extraction to distinguish malignant and benign masses. The features include shape of the mass, posterior acoustic behavior, radial gradient or margin, variance or autocorrelation, contrast, distribution of the distortions and many others [68]. Survey [69] reports 17 texture features, 17 morphological features, 10 model based features and 13 descriptor features.

Recent advances in the US segmentation include fusion of the medical images [70], using graphic processing units [71], multi-atlas segmentation [72], incorporating priors [73] using the AI methods combined with snakes [72, 74-76], advanced level set methods [28, 29, 77-82] and the multi-scale approach [83]. The US image analysis is a part of the computer assisted diagnostic systems. The entire evaluation includes mammography (usually the primary step), thermography [84, 85], Doppler imagery [3, 4] and elasticity analysis [5]. Such evaluation along with the computerized cytology [86, 87] constitutes a basic architecture towards the ultimate goal of fully

automatic clinical decision support systems for detection and grading of the breast cancer [88].

Active contours or snakes originally introduced by Kass et al. [8] is one of the most popular techniques for extraction of complex objects from digital images. Since the seminal work of Kass and colleagues, active contours have been applied to many object extraction tasks with differing degrees of success (e.g. survey [89]). Further improvements process the underlying vector field which moves the snake towards the required boundary, such as the gradient vector flow (GVF) [10, 90] and the generalized gradient vector flow field (GGVF) [11]. Some variations of these ideas are the multidirectional GGVF [91] and the non-linear diffusion model [92]. Recent modifications are the Convolution Vector Flow [33], Poisson Gradient Vector Field [16, 93], Segmented External Force Field [94], Dynamic Directional Gradient Vector Flow [34], Normal Gradient Vector Field [30], Priory Directional Information Vector Flow [95], Adaptive Diffusion Flow [35], Multi Feature Gradient Vector Flow [36], and Divergence Gradient Vector Flow [96].

A competing approach called the level set method (LSM) [97] is based on the ideas proposed by Osher and Sethian [98] to use a model of propagating liquid interfaces with curvature-dependent speeds. The LSM combined with the contour energy minimization resulted in a variety of the so-called geodesic deformable models [99-102]. However, the LSM makes it difficult to impose arbitrary geometric or topological constraints on the evolving contour via the higher dimensional hyper surface. Besides, the level set models may generate shapes having inconsistent topology with respect to the actual object, when applied to noisy images characterized by large boundary gaps [103] and non-closed curves [94]. Besides, the LSM is computationally expensive since it requires to propagate a 2D object (the level set surface) in the 3D space whereas the active contour methods evolve a 1D object (the closed contour) in the 2D space.

Numerous research papers apply the active contours to medical images. The examples are multi-direction snakes: skin cancer images [91], topology-adaptive snakes: MR brain images and CT scans [104], gravitational force snakes: a variety of medical and

non-medical images [105], narrow-band snakes: MRI and CT scan images of lungs [106], distance snake [107], GVF snake, balloon snake [108], "area and length" snakes [100], geodesic snakes [99], constrained snakes [101] and level set method: MRI, CT and US images of brain, liver, kidney [102], region-competition snakes (originally [109]): CT scan slices of arteries [110], sectored snakes [111] : abdominal CT scans [112], parametric snakes: US of breast masses [113], 3D-snakes: US breast cancer images [64, 113], GVF snakes with an edge map pre-processing: US of the liver tumors [114], GVF snakes combined with the region growing and the median filter: US breast tumors [115], sketch-snakes [64]: chest X-ray images [64], combination of snakes and active shape models: US of the human heart [116], the early-vision and the discrete-snakes: the US images [117], multi-resolution snake: echographic and echo brachial images [118], GGVF snakes combined with a continuous force field analysis: breast tumors in the US images [119], geodesic snakes and coupled geometric snakes: female pelvic organs in the MRI images [120-122].

Although, the snakes are widely used for detecting the objects of interest in various medical images. The success of snake-based segmentation strongly depends on the initialization. The inappropriate initialization may produce incorrect results.

2.5 Initialization Methods for GVF-type Parametric Snakes

One of the popular ideas is analysis of the vector field generated by the GVF-type model. For instance, [94] applies force field segmentation (FFS) to divide the image domain into disjointed regions representing the capture range of the external force field. The snakes can be individually initialized within each of the enclosures and moved to the targeted object boundary within it, avoiding being attracted by other objects. However, the algorithm transforms the image segmentation problem into a vector field segmentation problem, which is difficult to solve if strong noise is present.

10

The idea to initialize the snakes at the centers of divergence (CoD) of the GVF-type vector field was first mentioned in [123]. Further, Xingfei and Jie [20] define the CoD by analyzing relative directions of the vector field in a sliding 2x2 window (a generalization to larger windows is not available). He et al. [38] uses PPA [25] to detect the critical points of the vector field and a rule that "the initial contours should be set to contain all of the node points in the object area and none of the others". Although PPA has been used in a variety of image processing applications, e.g. [21, 23-27], the standard PPA classifier based on "if then" rules often can not be adapted to the case of snake initializations characterized by irregular nodes corrupted by noise. Moreover, neither [20] nor [38] differentiate the external and internal snakes. As a result, the image produced by [20] requires a special merging procedure to remove pseudo-boundaries appearing due to the over segmentation. Further, [38] uses only seeds characterized by a certain gray level associated with the object. Therefore, the method fails on low contract images characterized by shadows and artifacts such as the US images of breast cancer.

The similarity of the GGVF and the Navier-Stokes equations makes it possible to use the analogy of a flow through a porous medium. Consequently, [124] treats the initial snakes as sources of the flow emitting normal unit vectors on the image domain. The authors also noticed critical points of the flow and proposed to merge multi-snakes initialized around those points for segmentation of the MRI images of lungs. However, the method works only when the snakes are initialized inside the lungs. Although for these types of medical images such initialization is trivial, it is not the case for low contrast images such as the US images of breast cancer.

A competing idea is placing the seed points uniformly or randomly over the entire image, evolving the snakes from each seed point and analyzing the resulting configuration. For instance, [125] runs snakes until their convergence to a local minima and constructs a pattern image (an annular band around each snake). Next, the algorithm projects each pattern image into an already trained principal component classifier. The snakes associated with a lower reconstruction error are classified as objects and others as non-objects. However, the required classifier to validate the final configuration must be trained. Besides, classification of randomly initialized snakes is

computationally expensive and might lead to considerable inaccuracies. The final configuration depends on the relative speed of the snakes' evolution (time step) which is set up manually. Therefore, the final configurations can differ considerably.

Another interesting approach is the quasi-automated initialization (QAI) method by Tauber et al. [15, 126]. The method employs CoDs, combined with a tracing procedure to create a "skeleton" of the object, consisting of centers of strong and weak divergence. The centers of weak divergence are the points where the vectors of the GVF diverge in one (either horizontal or vertical) direction. The centers of strong divergence feature both horizontal and vertical divergences. The initial snake is generated around the skeleton. However, the initialization is not entirely automatic. The algorithm still requires at least one manually generated point inside the object. Moreover, in some cases the skeleton can evolve outside the boundary of the object.

Poisson Inverse Gradient Vector Flow (PIG) [127] establishes a relationship between the external force field and the underlying external energy field via the solution of the corresponding Poisson equation. The isoline of the minimum energy is selected as the initial contour. The model has been applied to the 2D and 3D cases for a variety of medical images. However, the method may suffer from incomplete isolines, as well as from over segmentation.

An automatic initialization method has been proposed in [16] for PET images of the liver. The candidate contours are generated by Canny edge detection and subsequently classified by a genetic algorithm. The algorithm has been applied to segmentation of face contours in video files [128]. A similar idea was introduced in [129] for detection of the synovial boundaries in US images. However, the proposed initial snakes selected from the edge map are not robust and may not be applicable to multiple objects.

The initialization algorithms for the US images often rely on gray levels and textures to place the seed points inside the tumor [17-19]. Saliency and feature maps have been proposed in [130]. [131] introduces a special vector field to hybridize the GVF and the texture. A Chan–Vese type model is proposed in [132] generates an initial

contour in the framework of region based segmentation. A few papers related to a specific medical image processing task use the typical position of a human organ in the US images (see, for instance, [133]). However, these models are image dependent and may not work if strong noise is present.

However, the existing initialization models for snake based segmentation are image dependent and may not work if a strong noise is present. Therefore, two new initialization algorithms are presented in Chapters 3 and 4.

2.6 Conclusions

The problem of initialization is in fact a problem of a rough segmentation. That is why the most popular method of initialization is manual. One of the most important problem is to determine whether the initial contour or multiple initial contours are located inside or outside the object of interest (the tumor in our case). Contours which partially located inside and partially outside the tumor are unacceptable or difficult to treat. The problem of initialization is not a specific problem of active contours. A good initialization method can be applied to level set methods [14], region growing [63], clustering [61, 62], watershed algorithms [58] and other segmentation methods.

As far as the US images are concerned, the proposed algorithms can be generalized to all types of breast abnormalities such as fibroadenoma, cyst, etc. Although there are some specific features attributed to these specific abnormalities, the proposed method will work with minor modifications.

Chapter 3
Trial Snakes Model

3.1 Introduction

It is critical to differentiate the snake's seeds initialized inside and outside the object of interest. Obviously, if one can do it for every position in the image, it means that the object has already been segmented. However, it is sufficient that the algorithm does it only for some points for which such differentiation is possible.

Our solution is based on trial snakes (TS) initialized around false objects and false edges so that they do not get attracted to them during their evolution (Figure 3.1 (c)). The proposed TS model combines the idea of vector field analysis [20] and multiple competing active contours [16]. The TS differentiates the internal and external seeds by checking their intersections with the boundary of the image. The basics of the TS have been published in [140]. This chapter presents an extended version of the TS paper.

3.2 Methodology

Our methodology is based on numerical experiments tested by ground truth hand drawn by the experienced radiologists. The accuracy measures are the Hausdorff distance (contour-based measures) and conventional region-based measures.

3.2.1 Seed Classifier

We propose a modification of classifier (2.3) (see [39], [40]) given by

$$C(\lambda_1, \lambda_2) = \begin{cases} \dfrac{\min(|\lambda_1|, |\lambda_2|)}{\max(|\lambda_1|, |\lambda_2|)} \dfrac{sign(\lambda_1 \lambda_2) + 1}{2}, & \text{if } \lambda_1 > \delta, \lambda_2 > \delta, \\ 0, & \text{otherwise.} \end{cases} \tag{3.1}$$

where δ is a threshold to exclude ill conditioned matrices characterized by small eigenvalues. The term $\dfrac{\min(|\lambda_1|,|\lambda_2|)}{\max(|\lambda_1|,|\lambda_2|)}$ includes converging/diverging configurations, i.e. attracting and repelling stars (see Table 2.1). The term $\dfrac{sign(\lambda_1\lambda_2)+1}{2}$ excludes the saddle points. All other patterns get a 0 score. The converging/diverging configurations are differentiated by the sign of the eigenvalues. Since GGVF eventually eliminates small groups of noisy pixels, the seeds must be initialized around large or medium size stars and nodes. Therefore, the PPA is combined with a growing window as follows:

$$\text{if } C(\lambda_1,\lambda_2)_k > \Delta\,, \lambda_1 > 0, \lambda_2 > 0,\ \text{for every } k = k_1,...,k_5\,, \tag{3.2}$$

where k is the size of the growing window and Δ is the suitable threshold to detect the large configuration, then the window is a candidate to be the seed.

Our numerical experiments show that $\delta = 0.001$ and Δ between 0.7 and 1.0 are appropriate for efficient detection of the seeds.

3.2.2 Algorithm of the Trial Snakes Model

The TS is based on the idea that if we detect all the converging and diverging stars inside the object and run the expanding snakes from them, they will eventually merge and attach themselves to the boundary (in case of attracting star the vector field must be inverted). Let N_D and N_C be the number of the diverging and converging stars respectively. The first stage of the algorithm is then given by the following pseudo-code:

15

```
void Evolve_the_Snakes(int i)
{
    Initialize a snake $S_i$ around the diverging star $D_i$. The snake is initialized as a

        circle inside the maximum window satisfying $C(\lambda_1, \lambda_2)_k > \Delta$.

    Evolve $S_i$ until it converges. If $S_i$ touches the image boundary, smooth the vector field inside

            the resulting contour.

    Exclude $D_i$ from the set of the diverging stars.

}
void Process_VectorField(void)
{
    do{

        Detect_all_Diverging_Stars $D_i$    //use classifier (3.1)

        Evolve_the_Snakes ( $N_D$ )   // call Evolve_the_Snakes $N_D$ times

    }while the number of diverging stars does not change and every snake converges
            to the same position.

}
void main(void)   // the program body
{
    do {

        Process_VectorField()
        Invert_the_vector_field   //The converging stars become diverging.
        Process_VectorField()

    }while every $S_i$ does not converge to the same position.

}
```

The algorithm is illustrated in Figure 3.1 and Figure 3.2. The first stage eliminates the seeds positioned outside the object. If a snake reaches the image boundary, the algorithm smoothens the vector field inside the contour to give the way to the snakes, which would have been blocked otherwise. The iterative procedure eventually excludes every external star (converging or diverging) leaving the internal stars intact (see Figure 3.1). When the vector field gets inverted e.g., $V_{inverted} = -V$, the converging snakes become diverging, so that they are grown on $V_{inverted}$ until they meet vectors in the opposite direction. When they stop, they get offset and then are grown further on the original vector field.
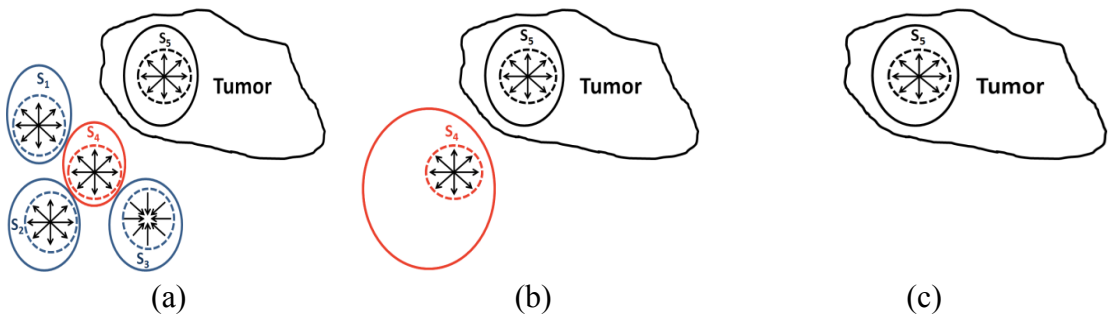
Figure 3.1 Elimination of the external stars, (a) S_4 gets blocked, (b) S_1, S_2, S_3 are eliminated, (c) S_4 is eliminated.
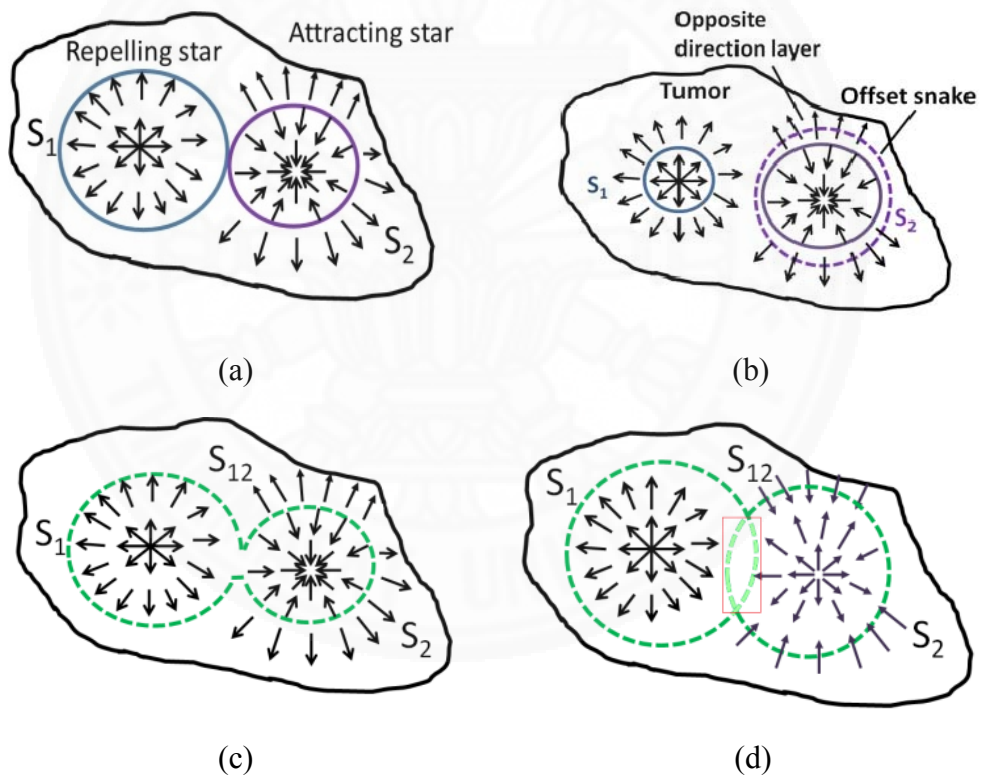
Figure 3.2 Multiple Snakes, (a) snake growing from a converging configuration "wakes up" a "sleeping" snake, (b) the offset snake picks up the opposite direction of the vector field, (c) merging of the growing contours, (d) merging of the intersecting contours.

17

Note that at the first stage merging is not allowed: if the external and internal snakes merge, the tumor becomes undetectable (see Figure 3.1 (a) - 3.1 (c)). However, when the external snakes disappear, merging becomes the basic mechanism of the proposed initialization. The algorithm runs on the original vector field, where the converging snakes are considered "sleeping", whereas the diverging snakes are growing and merging. Snakes S_1, S_2 merge whenever $dist_{H_1}(S_1, S_2) < \delta$, where δ is the merging threshold and $dist_{H_1}$ is the Hausdorff distance (see the definition in section 3.3). It is often the case that a growing snake merges with the "sleeping" snake and the resulting contour keeps growing (Figure 3.2 (a)). However, the algorithm does not guarantee that. Therefore, the converging snakes, which have not been "woken up" are offset by several pixels to pick up the repelling component of the vector field (Figure 3.2(b)). Note that for the converging configuration the small offset never intersects the boundary, since there is always a layer of vectors towards the boundary (Figure 3.2 (a)). The merging procedure generates a joint growing contour when the snakes are at the distance less or equal to δ (Figure 3.2 (c)) or when the snakes intersect due to initialization or due to excessive numerical step (overstepping). The algorithm includes detection of intersections and performs tracing to generate a joint contour, which becomes a new snake (Figure 3.2 (d)). The topological changes follow conventional split-and-merge procedures [104, 134, 135]. Besides our split-and-merge algorithm has been successfully tested on complex-shaped objects in [136].

Note that expanding from the inside of the object is not mandatory. In some cases it is acceptable to clean up all the converging and diverging configurations outside the object and initialize a contracting snake from the image boundary. However, the (tumor) generally has some homogeneity properties. Second, even though the smoothing process erases the attracting and repelling stars, the resulting vector field outside the tumor still could be chaotic and include false boundaries.

3.3 Performance Measures

In order to compare the proposed method with the conventional algorithms we introduce the following performance measures: the accuracy of segmentation result (contour-based and region-based), and the performance of the initialization procedure.

3.3.1 Contour Based Accuracy Measures

The snakes based segmentation is evaluated in term of the contour based similarity using the Hausdorff Distance. The distance (number of pixels) between the true contour (tumor ground truth hand-drawn by the radiologist) and the segmentation contour are measured as the following.

3.3.1.1 Maximum Hausdorff Distance

The maximum Hausdorff distance (H_1) given by

$$\text{dist}_{H_1}(X,Y) = \max\{\max_{a \in X} \min_{b \in Y} \| a - b \|, \max_{b \in Y} \min_{a \in X} \| a - b \|) , \qquad (3.3)$$

where $\| \ \|$ denotes the Euclidian distance, X the ground truth contour, and Y the resulting contour.

3.3.1.2 Average Hausdorff Distance

The average Hausdorff distance (H_2) obtain from dist_{H_1} by replacing the internal maximum by the average as the following equation

$$\text{dist}_{H_2}(X,Y) = \text{avg}\{\max_{a \in X} \min_{b \in Y} \| a - b \|, \max_{b \in Y} \min_{a \in X} \| a - b \|\} , \qquad (3.4)$$

3.3.1.3 Relative Hausdorff Distance

The relative Hausdorff distance (H_3) given by

$$dist_{H_3}(X,Y) = \frac{\text{dist}_{H_1}(X,Y)}{L_x} \xi , \qquad (3.5)$$

19

where L_X is the length of the true contour, and ξ is the normalizing coefficient. The distance allows evaluating the relative importance of the difference between the two curves. For instance, if $\text{dist}_{H_1}(X,Y)=10$, and $L_X=100$ pixels, the error is unacceptable, however, if for instance, $L_X=10000$, then dist_{H_3} is negligible.

The importance of the Hausdorff distance in comparing planar curves is that it is parametrization-invariant. Although dist_{H_1} is not a distance in a rigorous mathematical sense (it does not satisfy the triangle inequality), [137] shows that it is the best for matching the curved objects.

3.3.1.4 Contour-based True Positive Rate

The contour-based true positive is

$$TPR_c = \frac{TP_Y}{N_Y},\tag{3.6}$$

where TP is the number of true positive pixels, and N_Y is the total number of pixels belonging to the resulting active contour.

3.3.2 Region Based Accuracy Measures

3.3.2.1 Sensitivity

$$SEN = \frac{TP}{TP+FN},\tag{3.7}$$

3.3.2.2 Specificity

$$SPE = \frac{TN}{TN+FP},\tag{3.8}$$

3.3.2.3 Accuracy

$$ACC = \frac{TP+TN}{TP+TN+FP+FN},\tag{3.9}$$

where TP, TN, FP, and FN are the region-based true positive, true negative, false positive, and false negative.

Ref. code: 25605422300284YJH

3.3.3 Dice Analysis

Dice Similarity Coefficient (*DSC*) is defined by

$$DSC(A,B) = \frac{2*(A \cap B)}{A+B},$$ (3.10)

where *A* and *B* are the regions of the ground truth and the segmented result. The *DSC* is in the range of [0,1].

3.3.4 Performance of the Initialization Procedure

Observe that the accuracy measures introduced in Section 3.3.1, 3.3.2 and 3.3.3 are only supplementary because they depend on the segmentation engine. Therefore, the performance of the initialization is evaluated by

(1) Percentage of images for which the internal and external seeds were correctly detected: N_{corr}

(2) Percentage of images for which the contour was correctly segmented (the final snake is considered correctly if $\text{dist}_{H_2}(X,Y) \leq 3$), S_{corr}

3.3.5 Statistical Analysis

The standard deviation and the *p*-value are used to validate the significance of the numerical results.

3.4 Numerical Experiments

Our numerical experiments have been performed on 40 synthetic images, subjected to various levels of noise, and on 15 real US images of breast cancer. The method has been compared with a quasi-automatic initialization (QAI) [15, 126] based on detection of the centers of the weak and strong divergences. A special tracing procedure connects them, generating some kind of skeleton of the object. The skeleton snake requires one manually defined point inside the object (not fully automatic), whereas our procedure runs in an entirely automatic mode. Moreover, the

Ref. code: 25605422300284YJH

skeleton snake has not been properly tested against a series of real images. The impact of the noise was not evaluated and the accuracy of the segmentation has not been estimated. In this section, we show that skeleton initialization is sensitive to the noise and TS model outperforms this method in terms of the number of correct initializations and the accuracy.

We also compare the proposed initialization method equipped only with a basic version of GGVF with the Adaptive Diffusion Flow (ADF) [35], a recent version of the Level Set Method (LSM) [28, 77, 78] and an advanced version of the Fuzzy C-mean Clustering (FCM) [29, 79]. The proposed method outperforms the above algorithms even though we use the most basic GGVF (without any recent improvements).

The accuracy is measured by the Hausdorff distance between the resulting contour and the ground truth, by the percentage of true positives (*TP*) as well as by the sensitivity (*SEN*), specificity (*SPE*), accuracy (*ACC*) and dice analysis *(DSC)*. To compare the method with the skeleton snakes, we also use a binary measure counting the number of times when the initial snakes were correctly initialized inside the tumor. This allows to evaluate the true accuracy since an incorrect initialization can substantially decrease the average accuracy. On the other hand, even a correct initialization does not mean a good accuracy. Figure 3.3 (a)-3.3 (e) is an introductory example showing the skeleton initialization getting "distracted" by the inside converging configurations such a noisy "star" located nearby the boundary. (cf. correct segmentation by the TS in Figure 3.3 (f)-3.3 (k)). Furthermore, even when the initialization is correct i.e. positioned inside the tumor, it does not guarantee that the algorithm reaches the boundary. Figure 3.4 shows that the ADF, LSM and FCM may fail if the seed is initialized in a noisy area.

Finally, Figure 3.5 shows an example from Tauber et al. [15]. TS and QAI segmentations are practically identical, however, the skeleton snake requires one manually defined internal point whereas TS performs in an entirely automatic mode.

(a) noisy star   (b) ground truth

(c) QAI   (d) QAI   (e) QAI

(f) GGVF/PPA   (g) GGVF/TS   (h) GGVF/TS

(i) ADF/PPA   (j) ADF/TS   (k) ADF/TS
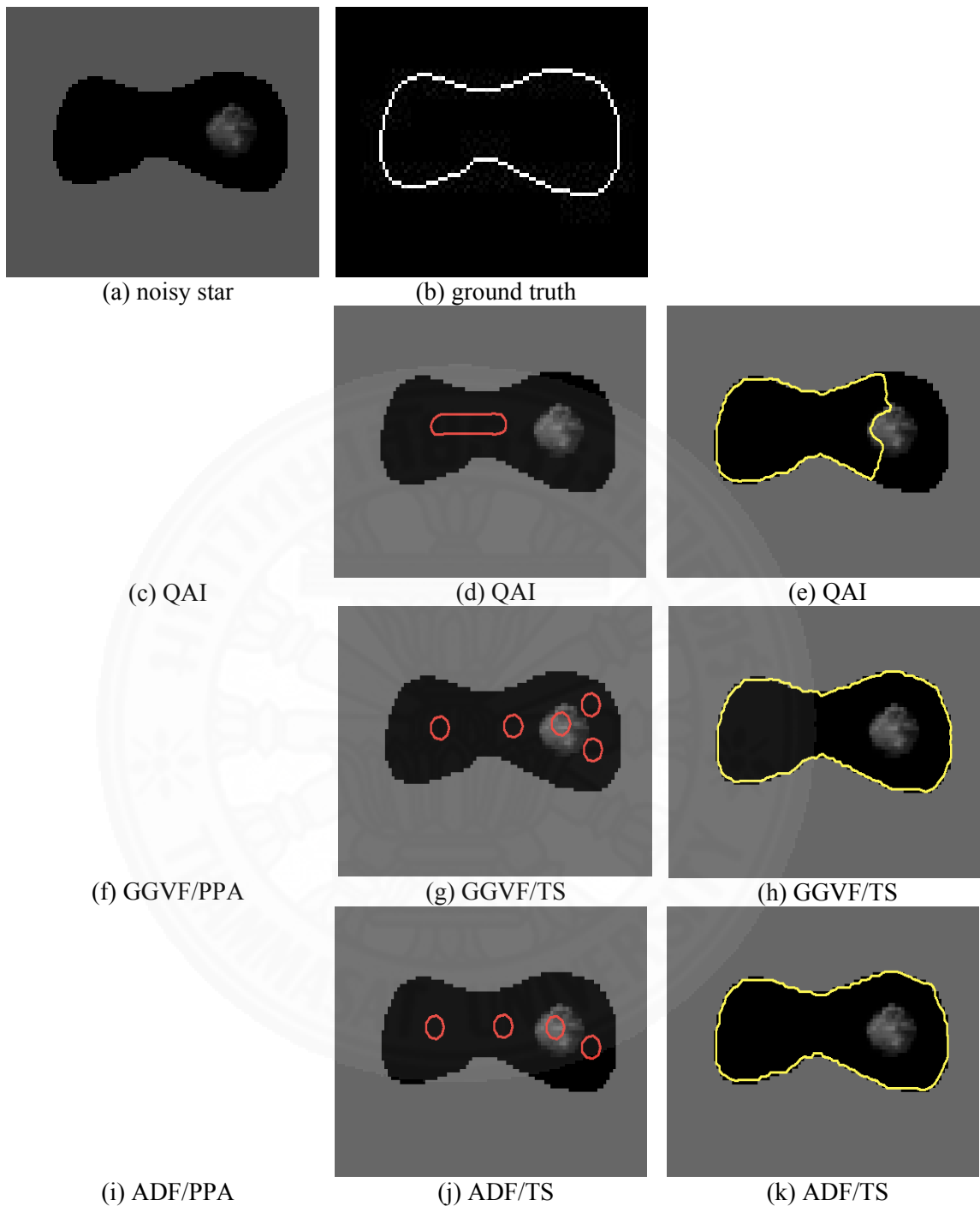
Figure 3.3 Introductory example QAI vs. TS initialization, (a) a synthetic tumor, (b) the ground truth, (c) QAI: strong and weak diverging points of skeleton snake, (d) Skeleton initialization, (e) skeleton snake: final contour, (f) GGVF and the corresponding stars, (g) TS initialization, (h) TS: final contour, (i) ADF and the corresponding stars, (j) ADF/TS initialization, (k) ADF/TS: final contour.
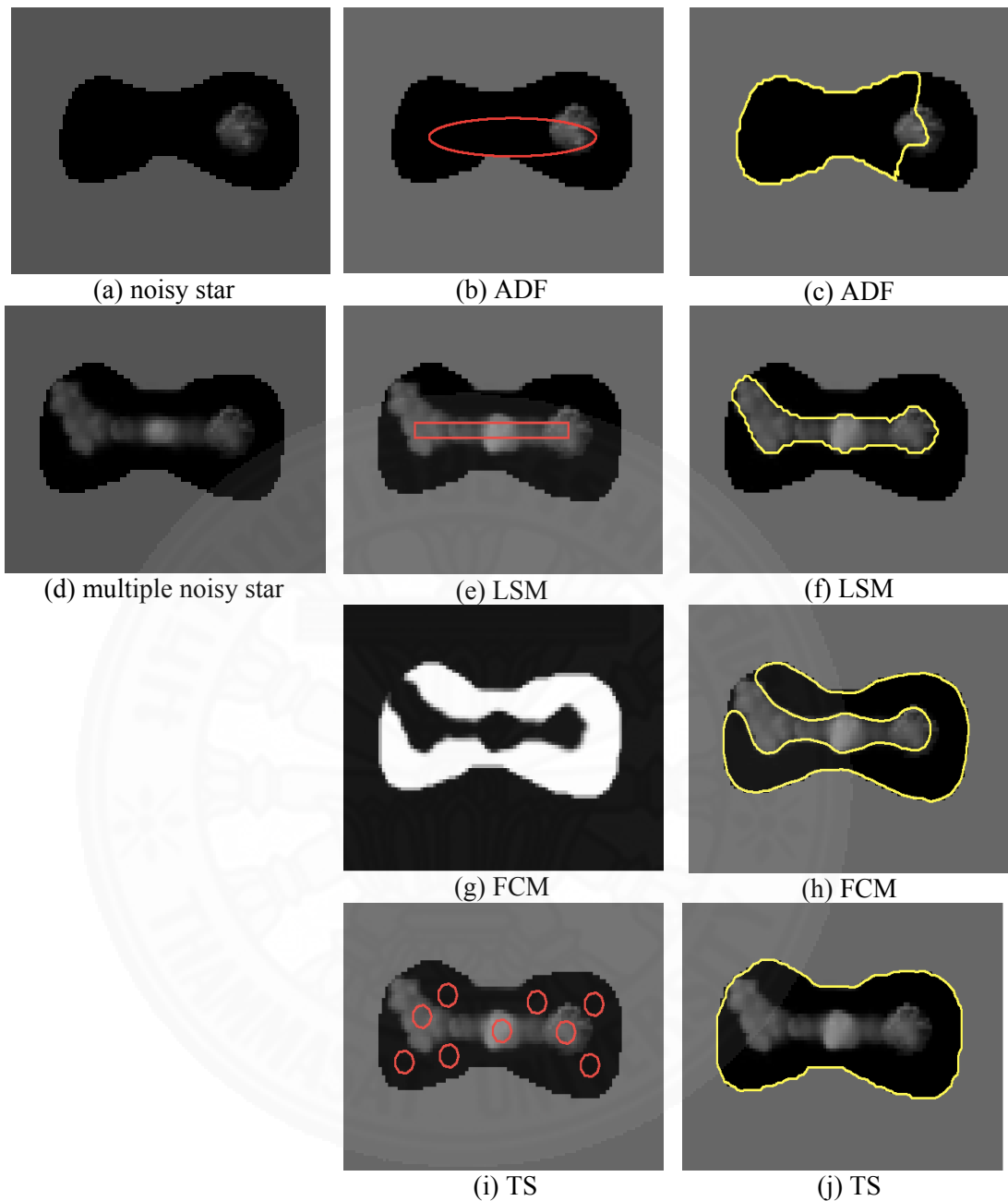
Figure 3.4 Introductory example TS vs. ADF, LSM and FCM, (a) Noisy star, (b) ADF manual initialization, (c) ADF final contour, (d) multiple noisy star, (e) LSM manual initialization, (f) LSM final contour, (g) FCM clustering, (h) FCM final contour, (i) TS automated initialization for the multiple noisy stars, (j) TS solution for the multiple noisy stars.

(a)   (b)

(c)   (d)
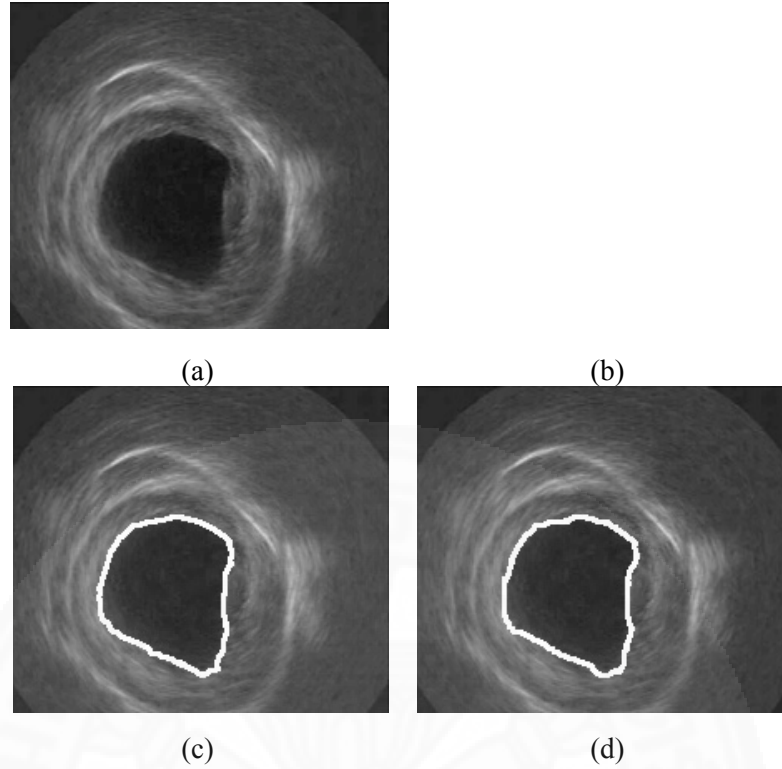
Figure 3.5 QAI example image, (a) US image from [15], (b) the vector field, (c) PPA segmentation, (d) Tauber's segmentation.

3.4.1 Example 1: Synthetic Images

We generate the synthetic tumors *visually similar* to the real US images. The visual analysis has been confirmed by the radiologists from Thammasat University Hospital. Forty (300x200) images of synthetic tumors were generated by using oval-like tumor shapes subjected to elastic deformations [139] and a trigonometric boundary noise (Figure 3.6). The images were degraded by the impulse noise and the additive Gaussian noise. The different levels of PSNR are: ∞ dB (no noise), 30 dB, 26 dB and 21dB (increasing noise). The images are characterized by a low contrast $c = \dfrac{G_{out} - G_{in}}{G_{out}} = 0.51$, where G_{in}, G_{out} are the average grey level inside and outside the synthetic tumor. Figure 3.6 shows an example of a typical synthetic image.

25

∞ dB   30 dB   26 dB   21 dB
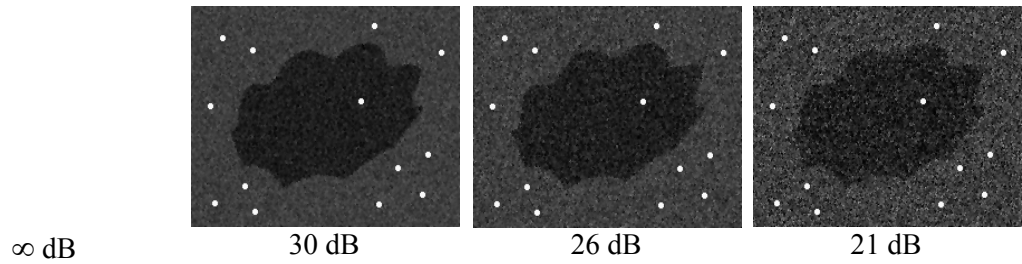
Figure 3.6 Synthetic tumors subjected to impulse and speckle noise.

Table 3.1 compares the competing methods in terms of the contour-based and region-based accuracy. The average accuracy was evaluated when the snakes were correctly initialized. The FCM runs with 3 clusters corresponding to the tumor, dark background and white shadow areas. The initial centers of the clusters are the average gray levels in these clusters. Since the FCM is a region based method, the final contour for evaluating H_1 was generated by the LSM [29, 79]. The initial contours for ADF, and LSM were generated manually in the noisy areas of the image. The area of the initial contour was about 60% of the total area of the tumor. Clearly, the TS has an overwhelming advantage with regard to QAI practically for every noise level. Even in the absence of the speckle noise (but with the impulse noise present) only 80% of the QAI are correctly initialized and only half of that 80% reaches the boundary. As far as the overall performance is concerned, the increasing noise level leads to a further decrease in the accuracy of the skeleton snakes. For instance, in case of 21 dB only 10% of the skeleton snakes are successful. The performance of the ADF snake with manual initialization is catastrophic with 0 correct segmentations at 21 dB, however, the LSM and FCM are comparable in terms of the number of correctly segmented images. The TS is consistently more accurate. Besides, the forthcoming Example 2 shows that TS outperforms the LSM and FCM in terms of the number of correctly segmented tumors in case of *real* US images. Finally, combining TS with the ADF does not lead to a substantial improvement. Moreover, in some cases TS/GGVF produces more accurate segmentation. This is because the standard deviation σ of a Gaussian smoother required for the ADF has not been tuned. We do not adjust it deliberately, otherwise, it won't be fair with regard to TS/GGVF which

26

does not use the Gaussian smoothing at all. We consider $\sigma = 0.5$ as recommended in [35].

Table 3.1 TS vs. benchmark methods for synthetic US images

Noise, dB	Model	Correctly initialized inside object, N_{corr} %	Correctly segmented, S_{corr} %	Accuracy						
				Contour-based Evaluation				Region-based Evaluation		
				H_1	H_2	H_3	TP	SEN	SPE	ACC
0	TS + GGVF	100	**100**	**2.10**	**0.73**	1.67	99.95	**99.80**	99.06	**99.33**
	QAI + GGVF	80	40	63.92	23.09	26.57	80.16	82.78	99.15	91.50
	TS + ADF	100	**100**	2.13	0.74	**1.57**	**100.00**	99.74	99.11	**99.33**
	LSM	Manual	80	12.46	5.49	3.32	79.91	81.25	99.59	94.97
	FCM	Manual	80	12.46	5.47	27.71	79.96	80.80	**99.93**	99.03
	ADF, 60 %	Manual	10	88.91	29.85	36.94	54.73	64.77	99.61	87.68
30	TS + GGVF	90	**90**	4.15	**1.46**	**2.60**	98.12	**99.32**	99.54	99.33
	QAI + GGVF	60	30	103.64	57.18	61.31	68.68	66.92	99.65	**90.38**
	TS + ADF	90	**90**	**3.79**	1.57	3.16	94.84	98.28	99.71	99.23
	LSM	Manual	80	14.08	6.14	4.09	78.78	80.40	99.96	94.88
	FCM	Manual	80	12.93	5.53	27.71	79.82	80.86	99.88	94.94
	ADF,60%	Manual	0	90.44	29.41	36.71	50.79	63.85	**99.89**	87.63
26	TS + GGVF	80	**80**	**4.53**	**1.67**	**3.23**	**95.37**	98.56	99.65	99.24
	QAI + GGVF	60	10	104.68	69.82	73.86	52.91	60.03	99.66	85.93
	TS + ADF	80	**80**	4.66	1.86	3.62	87.53	97.47	99.72	**98.94**
	LSM	Manual	80	15.47	6.33	4.30	77.01	79.91	**99.95**	94.69
	FCM + LSM	Manual	**80**	13.31	5.52	27.43	79.38	80.57	99.82	94.90
	ADF, 60 %	Manual	0	94.11	34.35	42.75	44.26	59.93	99.88	86.18
21	TS + GGVF	80	**70**	**9.42**	**1.98**	3.56	**88.00**	97.55	99.55	**98.73**
	QAI + GGVF	60	10	141.75	136.78	138.19	47.70	52.91	99.59	82.91
	TS + ADF	80	**70**	10.56	2.08	**3.51**	83.46	96.78	99.27	98.34
	LSM	Manual	**70**	19.81	6.67	4.60	71.38	79.10	**99.88**	94.33
	FCM	Manual	**80**	14.15	5.73	27.92	77.75	79.94	99.73	94.60
	ADF, 60 %	Manual	0	90.65	38.11	48.89	37.26	52.34	99.84	83.16

*The bold numbers indicate the best accuracy in each category

It should be noted that Table 3.1 and all further accuracy tables include only the cases when the contours have been correctly initialized. If the contour is initialized incorrectly, the resulting snake may collapse or even attach itself to the boundary of the image. In this case, the evaluation of the accuracy does not make sense.

3.4.2 Example 2: Ultrasound Images of the Breast Cancer

This section tests the TS against the QAI on a series of 15 US images of the breast cancer. The images have been obtained from Philips iU22 ultrasound machine available at Thammasat University Hospital. The ROIs have been outlined manually. The ground truth contours have been hand-drawn by three leading radiologists with

27

the Department of Radiology of Thammasat University. The final ground truth image was obtained using the voting overlapping score (two from three). The inter-observer variability of the dataset is 0.86 whereas the intra-observer variability is 0.92. The resolution of the images ranges from 200x200 to 300x400. Examples which demonstrate the advantages of the TS snakes applied to the real US images are shown in Figure 3.7 and Figure 3.8. Clearly the QAI, ADF, LSM and FCM fail when the tumor includes a large non-homogeneous area characterized by the noise and/or shadows. In this case the resulting contour may be attracted to false boundaries whereas TS avoids the false boundaries using multiple, properly initialized snakes.

Table 3.2 compares the performance of TS with QAI as well as with LSM, FCM and ADF. The initial contour for ADF, and LSM was generated manually so that the contour occupies 60% of the area of the tumor. Clearly, the TS outperforms the QAI due to its ability to detect the internal and external stars, avoidance of the noise and the use of multiple seeds, whereas the skeleton seed often grows outside the object or creates an incorrect skeleton which jeopardizes the entire initialization. Furthermore, FCM and ADF are apparent losers (60% and 46% respectively). The performance of LSM is somewhat acceptable, however, it segments correctly only 73% of the images, whereas TS generates 93% correct segmentations. Finally, TS scores the best in 8 categories from 9 (boldface numbers in Table 3.2).

(a) US image

(b) ground truth

(c) QAI

(d) QAI
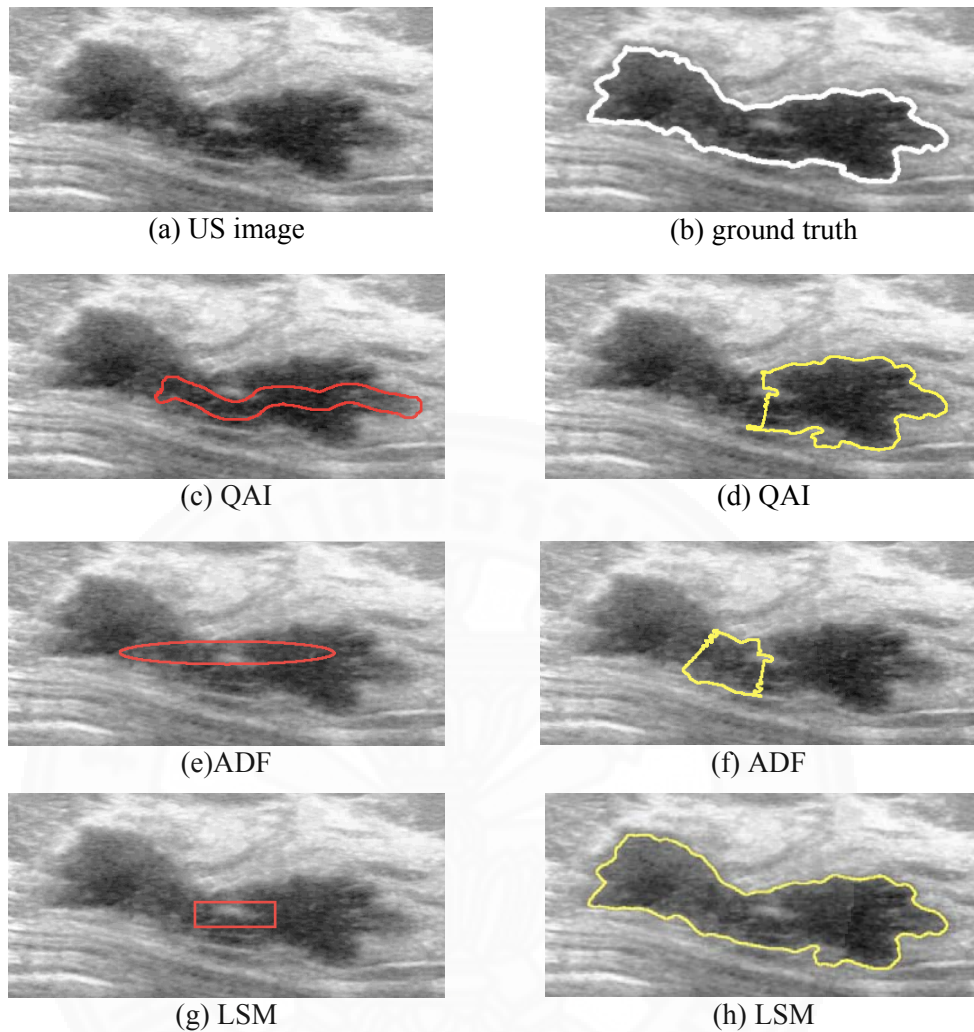
(e)ADF

(f) ADF

(g) LSM

(h) LSM

Figure 3.7 Real US example of TS vs. QAI, ADF, LSM and FCM, (a) US image,
(b) ground truth, (c) QAI skeleton initialization, (d) QAI final contour, (e) ADF
manual initialization, (f) ADF final contour, (g) LSM manual initialization, (h) LSM
final contour, (i) FCM manual initialization, (j) FCM final contour, (k) GGVF/TS
stars before elimination, (l) GGVF stars after elimination, (m) TS/GGVF
initialization, (n) TS/GGVF final contour, (o) TS/ADF initialization, (p) TS/ADF
final contour.

29

(i) FCM

(j) FCM

(k) GGVF/TS

(l) GGVF/TS

(m) GGVF/TS

(n) GGVF/TS

(o) ADF/TS

(p) ADF/TS
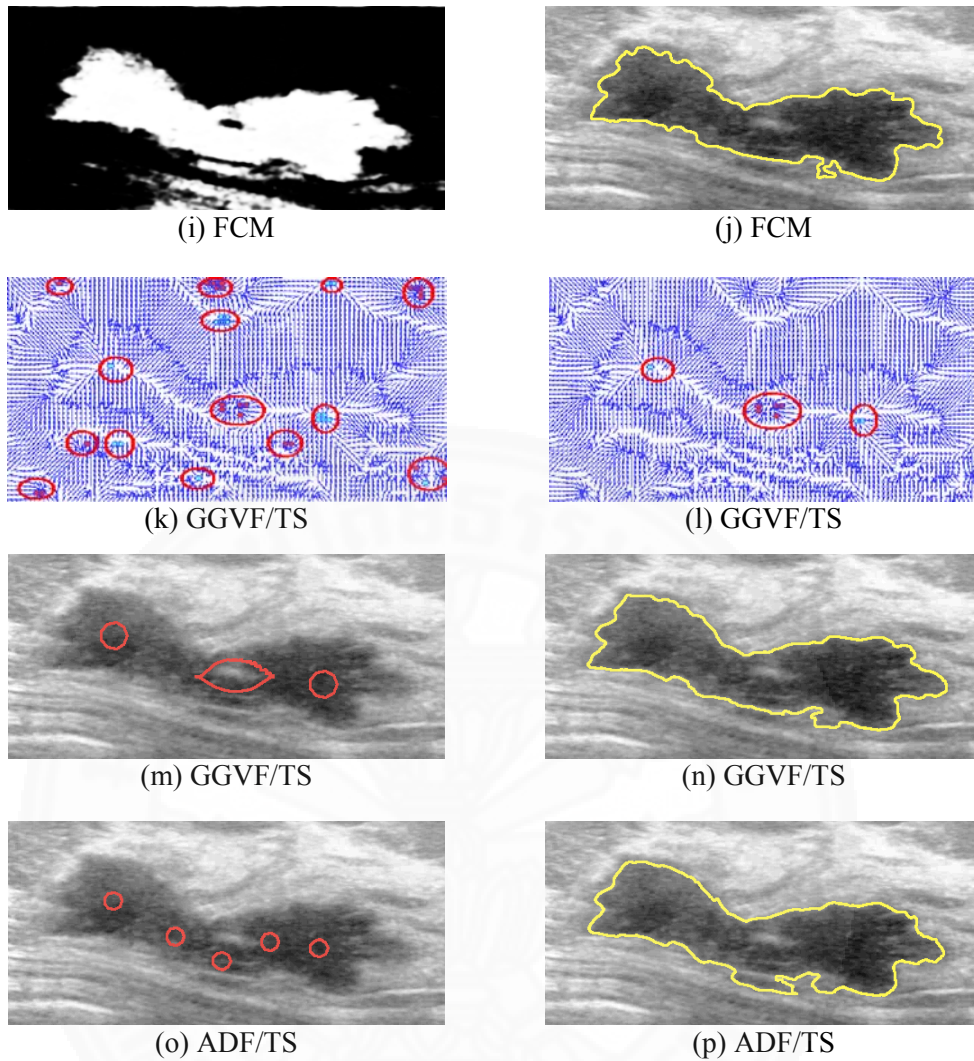
Figure 3.7 (Cont.) Real US example of TS vs. QAI, ADF, LSM and FCM, (a) US image, (b) ground truth, (c) QAI skeleton initialization, (d) QAI final contour, (e) ADF manual initialization, (f) ADF final contour, (g) LSM manual initialization, (h) LSM final contour, (i) FCM manual initialization, (j) FCM final contour, (k) GGVF/TS stars before elimination, (l) GGVF stars after elimination, (m) TS/GGVF initialization, (n) TS/GGVF final contour, (o) TS/ADF initialization, (p) TS/ADF final contour.

30
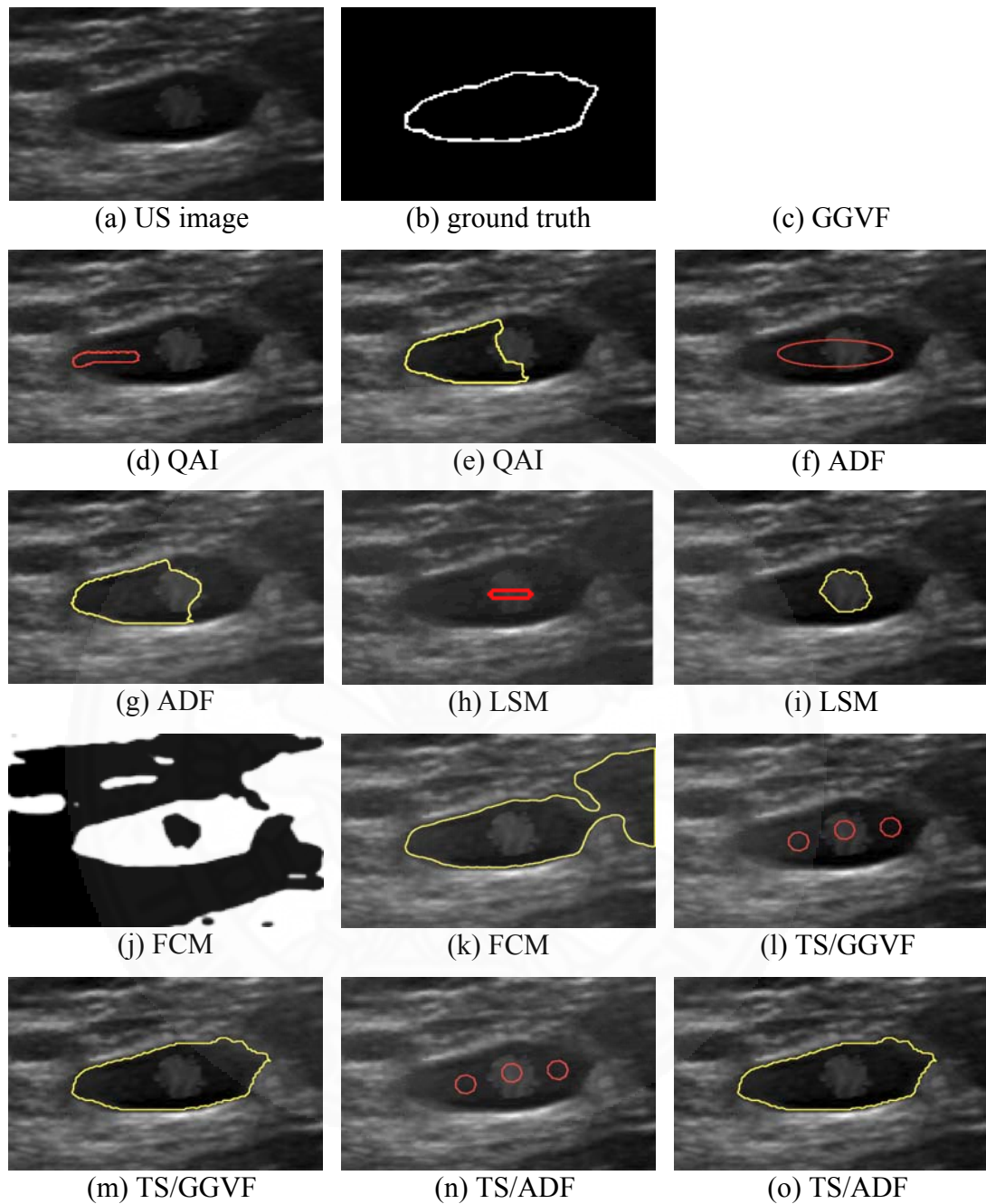
Figure 3.8 Real US with noise example of TS vs. QAI, ADF, LSM and FCM, (a) US image, (b) ground truth, (c) GGVF, (d) QAI skeleton initialization, (e) QAI final contour, (f) ADF manual initialization, (g) ADF final contour, (h) LSM manual initialization, (i) LSM final contour, (j) FCM manual initialization, (k) FCM final contour, (m) TS/GGVF initialization, (n) TS/GGVF final contour, (o) TS/ADF initialization, (p) TS/ADF final contour.

31

Table 3.2 TS vs. benchmark methods for real US images

Model	Correctly initialized inside object, N_{corr} %	Correctly segmented, S_{corr} %	Accuracy							
			Contour-based Evaluation				Region-based Evaluation			
			H_1	H_2	H_3	TP	SEN	SPE	ACC	DSC
TS + GGVF	**100**	**93.33**	**8.64**	**2.16**	3.15	89.66	94.50	99.67	**98.38**	**0.998**
QAI + GGVF	86.67	66.67	19.09	7.02	8.36	79.77	88.94	99.82	97.54	0.972
TS + ADF	100	**93.33**	8.54	2.13	**3.07**	**92.58**	**94.53**	99.54	98.25	0.988
LSM	Manual	73.33	38.81	21.25	22.63	66.81	69.77	99.54	90.11	0.939
FCM	Manual	60	25.43	4.93	6.59	76.19	92.10	96.14	95.41	0.969
ADF	Manual	46.67	47.43	20.36	19.54	68.15	73.34	**99.91**	92.72	0.952

Further, Table 3.2 shows that the TS produces the highest Dice index. The corresponding Standard Deviation (STD) are shown in Table 3.3. The STD for the region based measures is excellent, although, it is comparable with the mean for the contour based methods. However, 70% of the samples lie in the interval [Mean-STD, Mean+STD] which indicates a small error. Note that it also complies with the hypothesis of the normal distribution. Finally, the *p*-values which are less than 0.05 for every measures (Table 3.4) show that the results are statistically significant although the number of images is relatively small. The failed cases include the snakes which either attach to the false boundaries created by the noise, self-intersect of attach to the boundary of the image.

Table 3.3 The mean and STD of TS model

Statistical Analysis	Average accuracy							
	Contour-based measures				Region-based measures			
	H_1	H_2	H_3	TP	SEN	SPE	ACC	DSC
TS+GGVF								
Mean	8.64	2.16	3.15	89.66	94.50	99.67	98.38	0.998
STD	3.80	0.75	1.69	9.45	3.66	0.45	0.73	0.006
TS+ADF								
Mean	8.54	2.13	3.07	92.58	94.53	99.54	98.25	0.988
STD	3.96	0.57	1.44	6.86	3.66	0.45	0.73	0.006

Table 3.4 The *p*-values of the TS model

Model	*p*-values
TS+GGVF	0.048
TS+ADF	0.012

3.5 Limitations of the method

The algorithm has been designed and implemented for the case of a single object (a malignant or benign tumor in the US images). The case of multiple objects needs further modifications. Furthermore, in the case of very noisy images characterized by a low contrast, the TS trial external snake may get stuck inside the image and may not reach the boundary at all. A possible extension is a combination of the proposed multiple growing snakes initialized inside the US image and sequence of contracting balloon snakes [108] initialized at the boundary of the image characterized by a varying balloon force.

3.6 Conclusions

The proposed automatic procedure for initialization of snakes for segmentation of the US breast cancer images (TS) shows an excellent performance as applied to synthetic as well as to real US images. It outperforms a recently proposed quasi-automatic method (skeleton snakes). The proposed initialization method equipped with the most basic version of GGVF also outperforms the Adaptive Diffusion Flow, an advanced Level Set Method, and a Fuzzy C-mean Clustering combined with the Level Set Method. The numerical experiments show that in many cases the conventional algorithms do not reach the actual boundary due to inappropriate initial positions of the seeds.

33

Chapter 4
Exploding Seeds Model

This chapter presents the Exploding Seeds (ES) method for automatic initialization of parametric active contours. The basics of the ES have been published in [141]. This chapter presents an extended version of the method.

4.1 Introduction

The TS introduced in Chapter 3 is characterized by high accuracy, however, the most serious drawback of TS is a considerable amount of computational time.

Therefore, we propose an extension of TS (Trial Snakes). The new fast algorithm for automatic initialization combines PPA [20], multiple active contours [16, 140], and the walking particles generated by the exploding seeds. It should be noted that the idea of using walking particles for edge detection has been proposed in [42]. However, their use for snake initialization has been totally overlooked. Besides, [42] employs "*charged*" particles which attach themselves to the edges. As opposed to that, our proposed particles bounce off the edges, which creates a totally different model suitable for fast initialization. The proposed bouncing particles are also different from the evolutionary algorithms, such as the ant colony or fireflies, since they do not employ any selection, competition, or other intricate components of the bio-inspired models which slow down the computations. Although modifications based on artificial intelligence (AI) are possible, they are out of the scope of this dissertation.

This proposed algorithm decides whether the seed is inside or outside the object of interest (tumor) as follows: the initial seeds simultaneously "explode", generating a set of particles moving initially along a radial direction relative to the seed. The velocity of the particle is subjected to random fluctuations, which prevent them from entering into repeated (cyclic) trajectories (see Section 4.2). The key feature of the model is that the particles bounce from the strong edges. Therefore, the particles

34

generated inside the object (tumor) stay inside, whereas those generated outside the tumor, reach the boundary of the image and disappear. The particle model is faster and more accurate than the TS [140]. This is because the TS may get stuck between the edges or inside the cavities, whereas the particles will eventually find their way to the boundary of the image.

The ES has been tested against five state-of-the-art models mentioned in Chapter 2 and Chapter 3, namely, TS [140], FFS [94], CoD [20, 38], QAI [15, 126], and PIG [16]. With regard to the above benchmark methods, the ES provides fast and accurate initializations, which in turn lead to more accurate segmentations. The algorithm might be used in a framework of other segmentation methods such as the level set method, hieratical clustering, etc., however, combining ES with the above conventional techniques is out of the scope of the thesis. A video demonstration of the ES algorithm is at http://onlinemedicalimages.com/index.php/en/presentations

4.2 Methodology

4.2.1 Phase Portrait Analysis

The first step of ES, we use the PPA based classifier (3.1) to detect the big attracting and repelling stars, as well as strong attracting and repelling nodes (see Table 2.1) similarly to TS. The walking particles are initialized around these stars. The points that are classified as an "edge" (a true or a false boundary in Table 2.1), are considered as the "walls" from which the walking particles bounce off.

4.2.2 Exploding Seeds

The seeds are initialized around each repelling or attracting star detected by PPA based classifier (3.1) or a group of stars merged together. The proposed algorithm decides whether the seed is inside or outside the object of interest (tumor) as follows: the initial seeds simultaneously "explode", generating a set of N_p particles moving initially along a radial direction relative to the seed (see Figures 4.1 (a), 4.1 (b)). The velocity of the particle is subjected to random fluctuations, which prevent them from

35

entering into repeated (cyclic) trajectories. The key feature of the model is that the particles are bouncing off the internal and external edges and disappearing (dying) at the boundary of the image (Figure 4.1 (c)). Those initialized inside the tumor stay inside, whereas particles initialized outside eventually find their way to the boundary of the image and subsequently get deleted. Finally, since the majority of the surviving particles belong to the inside seeds, this efficiently differentiates the external and internal seeds (Figure 4.1 (d)).
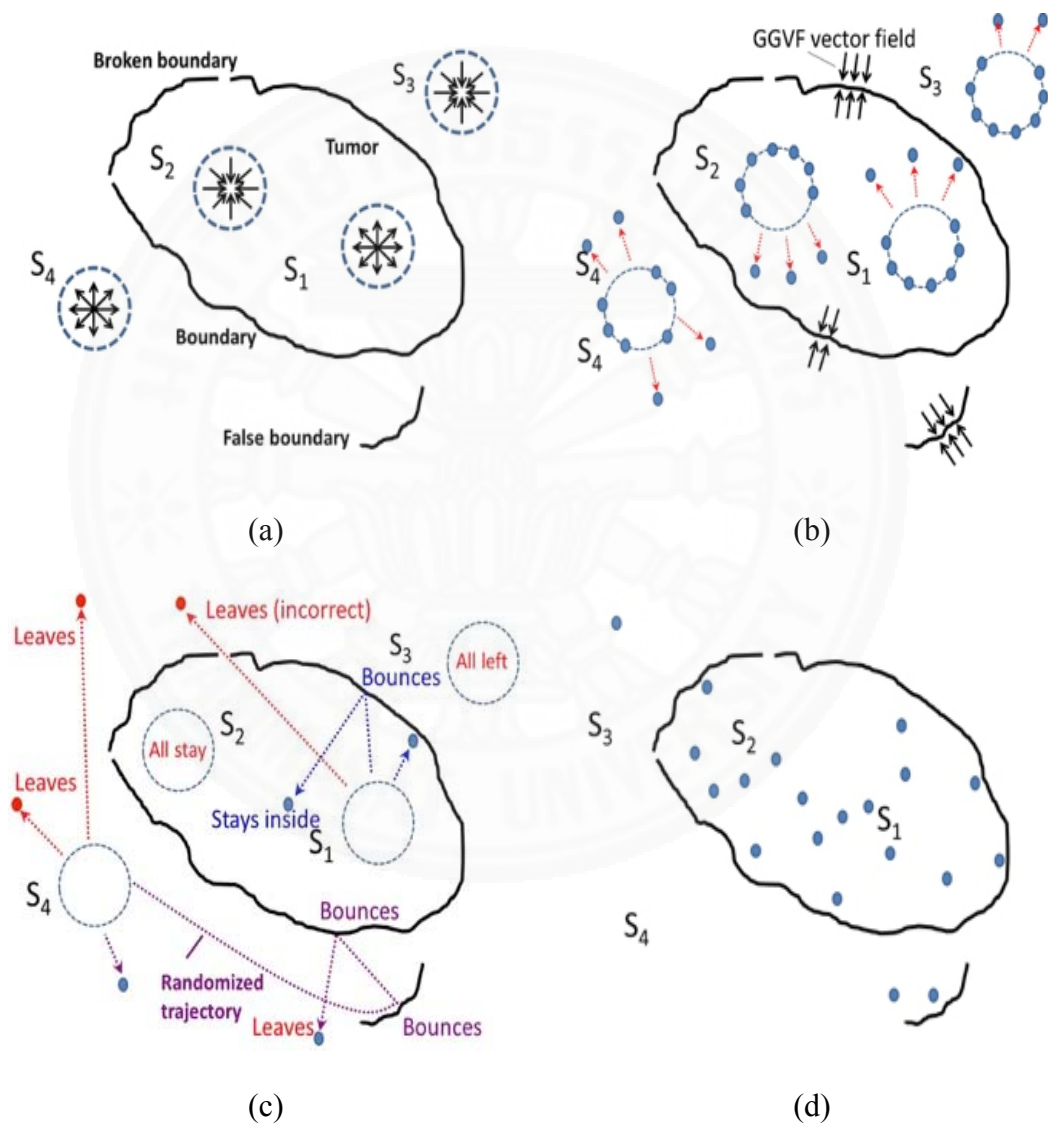
Figure 4.1 Elimination of the external seeds, (a) seeds initialized, (b) seeds "explode", (c) walking particles, (d) the majority of the particles stay inside the object.

In order to avoid repeated trajectories (loops), the speed of each particle is subjected to small random perturbations (noise).

Let c_i be a center of an ith converging/diverging star. The velocity of a particle i, j is then given by

$$v_{i,j} = \alpha v_{d,i,j} + \beta v_{r,i,j}, \tag{4.1}$$

where α, β are weighting parameters. The initial deterministic component of the velocity is given by $v_{d,i,j} = \begin{pmatrix} \cos\dfrac{2\pi j}{N_p - 1} \\ \sin\dfrac{2\pi j}{N_p - 1} \end{pmatrix}$, $j = 0, ... N_p - 1$.

When the particle bounces off the edge

$$v_{d,i,j} = n_{i,j}, \tag{4.2}$$

where $n_{i,j}$ is the unit normal to the edge at the point of the collision. The normal is antiparallel to the GVF-type vector at the edge.

The trajectory $p_{i,j}(t) \equiv \begin{pmatrix} x_{i,j}(t) \\ y_{i,j}(t) \end{pmatrix}$ of the particle i, j is given by

$$p_{i,j} = c_i + v_{i,j} t, \tag{4.3}$$

before the first collision and by

$$p_{i,j} = e_j + v_{i,j} t \tag{4.4}$$

after a collision with the edge e_j, where t denotes the pseudo-time.

As already noted, using solely v_d produces repeated (cyclic) trajectories. The random component v_r prevents the model from entering into repetitions (see Section 4.4 for further discussion regarding the relationship between v_d and v_r). The particles may get stuck between two or more neighboring edges. Such particles are detected, deleted, and re-initialized.

When a particle reaches the edge, it bounces off in a direction normal to the edge. The incentive is that if the tumor is circular, the particles move towards the center, which reduces excessive bouncing. The numerical experiments show that this feature reduces the number of degenerate trajectories. Finally, in order to prevent the particles from leaving the tumor, v_j must satisfy: $|v_j| \leq \min T$, where T is the thickness of the edge. Therefore, on each step v_j is normalized, e.g. $v_{i,j,new} = \dfrac{Tv_{i,j}}{|v_{i,j}|}$.

The algorithm is terminated when the death rate d (the number of particles leaving the image) becomes sufficiently small (see Section 4.4 for details and discussion).

Finally, when the ES model is terminated by the stopping criterion, the seeds are classified accordingly to the total average lifetime $l_{i,j}$ of the corresponding particles. If $l_j \leq \Delta_l$, where $l_j = \sum_{j=1}^{N_p} l_{i,j}$ and Δ_l denotes the corresponding threshold, the seed is classified as external, otherwise, as internal. Our forthcoming numerical experiments show that the model endowed with appropriate control parameters separates the internal and external seeds for the US images with a 96.7% success rate.

4.2.3 Multiple Snakes

The next stage of the algorithm is multiple snakes evolving inside the tumor (Figure 4.2), similar to the last stage of TS (see section 3.2.2). Recall that, the snakes initialized around the converging/attracting stars grow along the inverted GVF-type vector field until they stop at the local region of noise or artifact inside the tumor. These snakes are re-initialized by offsetting them by several pixels to pick up the repelling component of the vector field and then they are merging with the snakes initialized around the diverging/repelling stars.

38

<center>(a)   (b)   (c)</center>
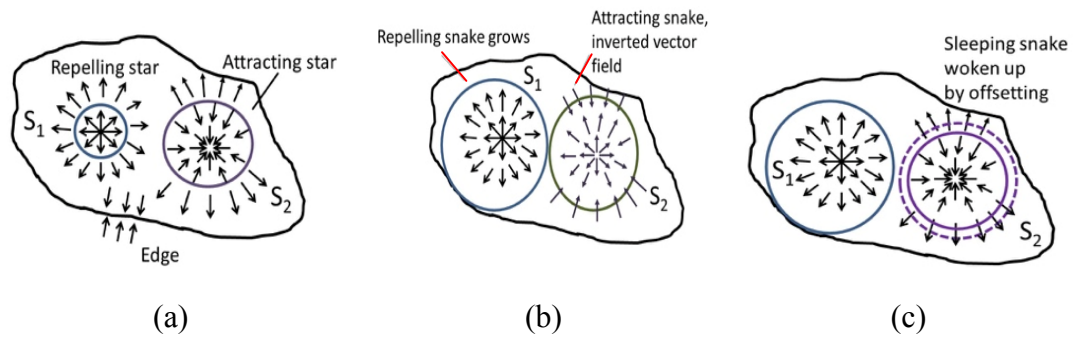
Figure 4.2 Snake evolution, (a) attracting and repelling internal stars, (b) attracting snake grows, (c) offsetting of the "sleeping" snake.

4.2.4 Algorithm of the Exploding Seeds Model

A pseudo-code of the initialization algorithm is given below, where delta1, delta2, and delta3 denote the corresponding thresholds. All other notations are self-explanatory.

```
void Vector_Field(void)
{ Evaluate the edge map f . }

void GGVF(void)
{ Apply the GVF to ∇f . }

void Find_Stars(void)
{ Using the PPA detect the converging and diverging stars. }

void Find_Edges(void)
{ Mark every saddle node (edge point) as Edge . }

void Merge_Stars(void)
{ Merge closely located stars. }

void Initialize_Particles(int iStar)
{ Initialize Nparticles particles on a circle around star i with the radius derived from condition (3.2). }

void Initialize_All_Particles(void)
{
    for (i=1; i<=Nstars; i++)
        Initialize_Particles(i);
}
```

<center>39</center>

```
void Move_Particle(int iStar, int jParticle)
{
    Position_Particle[iStar][jParticle]=Position_Particle[iStar][jParticle]+time_step*Velocity[iStar][jParticle] ;
    if (Position[iStar][jParticle]==Edge)
        Bounce_Particle(iStar, jParticle)
    else if (Position[iStar][jParticle]==ImageBoundary)
        Delete_Particle(iStar, jParticle)
    else
        Velocity[iStar][jParticle]=Velocity[iStar][jParticle] + Random_Component();
    Normalize_Velocity(iStar, jParticle);
}

void Move_All_Particles()
{
    for (i=1; i<=Nstars; i++)
        for (j=1; j<=Nparticles[i]; j++)
            Move_Particle(i, j)
}

int Death_Rate()
{ Count the number of particles deleted during the current step. }



void main(void)
{
    Vector_Field()
    while (Residual <delta1)
        GGVF();
    Find_Stars();
    Merge_Stars();
    Find_Edges();
    Initialize_All_Particles();
    while Death_Rate() > delta2
        Move_All_Particles();
    for (i=1; i<=Nstars; i++)
        if (Nparticles[i] >delta3)
            Initialize_Snake(i)
}
```

4.3 Performance Measures

In order to compare the ES with the benchmark algorithms we evaluate the performance of segmentation results in terms of the contour based accuracy and the region based accuracy measures (see sections 3.3.1, 3.3.2 and 3.3.3 respectively). We also evaluate the computational time.

The initialization performance of the ES are evaluated as following,

(1) Percentage of the images for which the seeds are correctly initialized as internal/external seeds: N_{corr}

(2) Percentage of the images for which the contour was correctly segmented: S_{corr} (the final snake is considered correct if $\text{dist}_{H_2}(X,Y) \leq 3$

(3) Computational time of initialization procedure: T_{comp}

As noted above, the segmentation accuracy depends not only on initialization, but on the segmentation model as well. For instance, the level set method, clustering, region growing, and edgeless active contours may benefit from the proposed TS and ES. However, this analysis is out of the scope of this dissertation. The model is limited to the parametric active contours, whereas the benefits of the geometric or level set methods may be precluded by this initialization.

4.4 Results and Discussion

The algorithm has been tested on 60 US images of breast cancer from 60 different patients obtained by a Philips iU22 ultrasound machine at Thammasat University Hospital. The ground truth contours have been hand-drawn by leading radiologists with the Department of Radiology of Thammasat University. The ground truth was obtained from three expert radiologists to check the inter-observer variability and intra-observer variability. The inter-observer variability value of this dataset is 1.91 whereas the intra-observer variability value is 1.12.

The ES has been tested against five state-of-the-art models, namely, TS [140], FFS [94], CoD [20, 38], QAI [15, 126], and PIG [16], using the performance measures introduced in Section 4.3. In order to prove the efficiency of the ES, we apply the recent Adaptive Diffusion Flow (ADF) method [35], which has been proven to be superior to GVF [90], GGVF [11], Normal Gradient Vector Flow [30], Infinity Laplacian GVF [31], Harmonic Gradient Vector Flow [32] and Convolution Vector Flow method [33]. We test the five competing initialization methods, considering the

41

ADF snakes as one of the best tools to perform segmentation, given a particular initial contour or a set of contours.

Figure 4.3 is an introductory example, comparing the initialization and the resulting snake produced by the ES with QAI, CoD, FFS, and PIG.
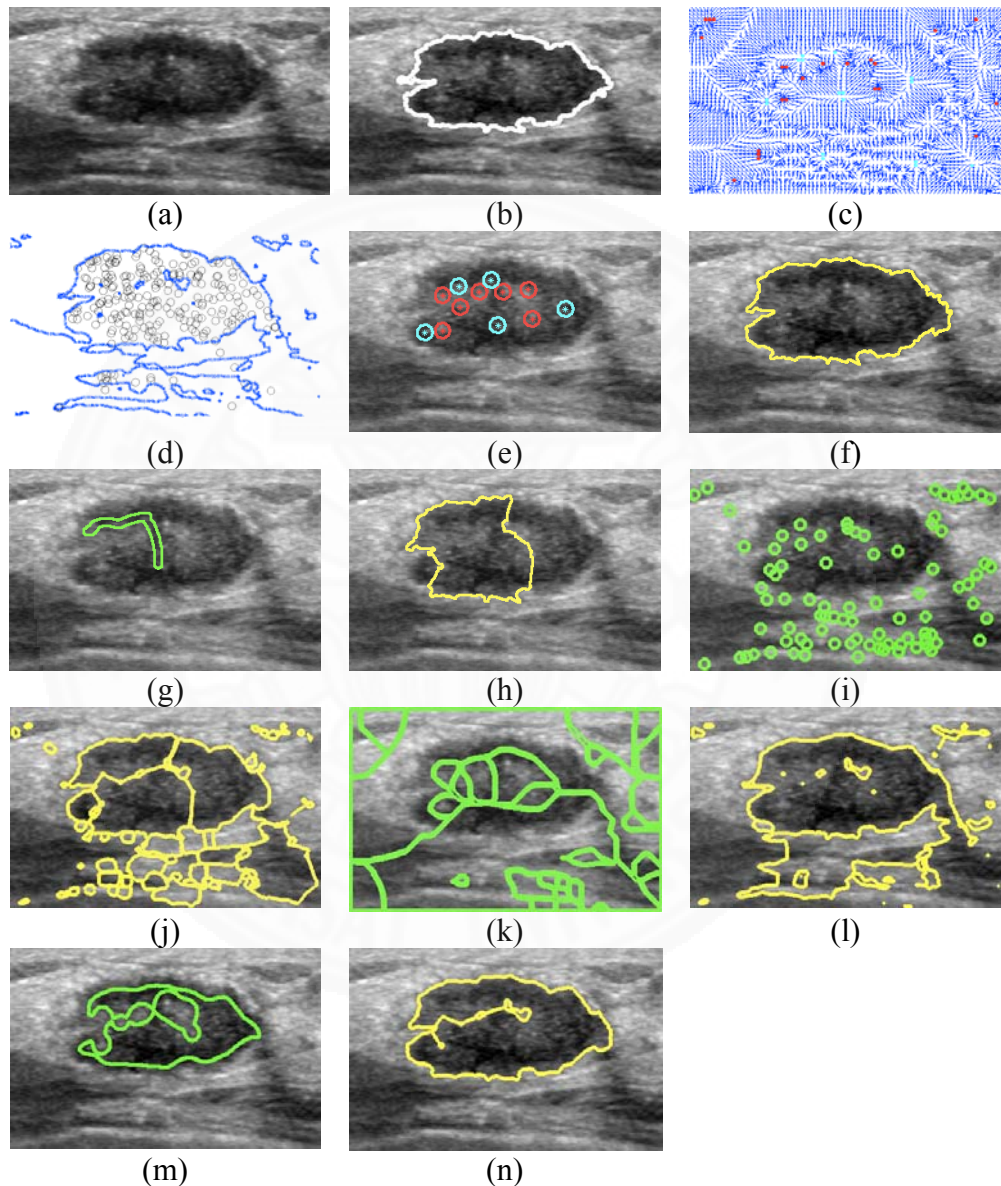
Figure 4.3 ES vs. Benchmark methods, (a) original US image, (b) ground truth, (c) vector field and stars, (d) walking particles detect the internal snakes, (e) ES initialization, (f) ES final contour, (g) QAI initialization, (h) QAI final contour, (i) CoD initialization, (j) CoD final contour, (k) FFS initialization, (l) FFS final contour, (m) PIG initialization, (n) PIG final contour.

42

Table 4.1 shows a numerical comparison of the ES with the above benchmark initialization methods performed on 60 US images. The CoD and FFS failed, whereas QAI and PIG yield a lower performance in both N_{corr} and S_{corr}. The ES initialization leads to a better segmentation accuracy. For instance, in terms of $dist_{H_3}$, the average accuracy of the ES is 3.06 pixels, vs. 13.69 and 6.53 for QAI and PIG, respectively. The ES also gives the best *DSC* (about 99%). The TS method is the only real competitor of the ES. The TS method produces approximately the same initialization results, however, the TS model is extremely slow relatively to the ES. Our numerical experiments show that the ES is approximately 10 times faster.

Recall that the velocity of the particle is given by $v_{i,j} = \alpha v_{d,i,j} + \beta v_{r,i,j}$, where α, β are weighting parameters corresponding to the random and deterministic component of $v_{i,j}$. The parameter β ensures that the particles do not enter cyclic trajectories, so that a majority of the external particles sooner or later leave the image. On the other hand, too large β leads to abrupt trajectories and slows down the model.

Table 4.1 Comparison of the ES with the benchmark initialization methods

Model	Correctly initialized, N_{corr} %	Correctly segmented, S_{corr} %	Average accuracy							
			Contour-based measures				Region-based measures			
			H_1	H_2	H_3	TP	SEN	SPE	ACC	DSC
ES	**96.7**	90	**10.38**	**3.59**	**3.06**	**83.77**	85.13	99.83	**96.41**	**0.989**
QAI	86.7	66.7	36.87	26.01	13.69	70.24	71.35	**99.84**	94.45	0.972
CoD	0	0	83.81	49.74	19.68	30.40	**95.51**	68.34	74.33	0.772
FFS	0	0	89.86	38.58	21.96	37.57	92.94	88.44	89.33	0.916
PIG	73.3	68.3	24.69	6.24	6.53	78.96	80.23	97.41	93.28	0.976

Consider a normalized velocity, i.e. $v_{i,j} = \alpha v_{d,i,j} + (1-\alpha) v_{r,i,j}$, $|v_{i,j}| = 1$.

Table 4.2 illustrates tuning the parameter α using 15 additional US images. The images were manually selected from *onlinemedicalimages.com* as follows: 5 images with a weak boundary, 5 images characterized by complex shaped boundaries, and 5 random images (see Figure 4.4). None of the images was included in our basic test set of 60 images.

<center>(a)   (b)</center>
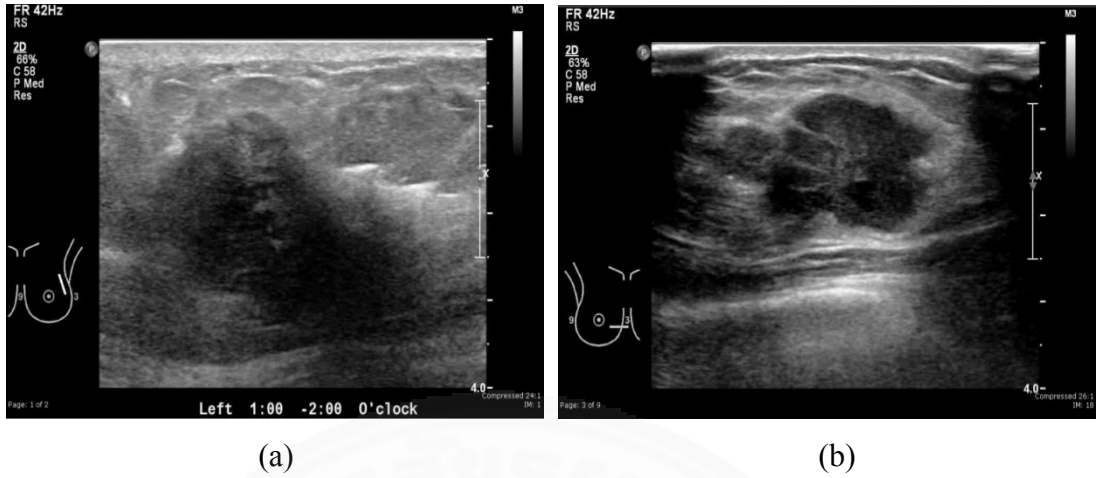
Figure 4.4 Examples of the US images selected for tuning the model, (a) weak boundary, (b) complex shaped tumor.

<center>Table 4.2 Deterministic vs. random component of the velocity</center>

α	S (# of iterations)	T_{comp} (computational time), sec
0.9	677	8.43
0.8	**634**	**7.78**
0.7	727	9.73
0.6	767	10.19
0.5	646	8.12

The model stops when 90% of the outside particles leave the image domain. Clearly, for this image collection, $\alpha \approx 0.8$, provides an optimal computational time.

Note that, although Table 4.2 gives us an idea about the range of the weighting parameter α, it is based on a very conservative stopping criterion. In practice, we do not know how many outside particles have left. As a matter of fact, the stopping criterion should be 1) independent of the total number of particles, 2) related to the number of the external particles, and 3) related to the size of the image.

<center>44</center>

Therefore, we introduce a stopping criterion based on the moving average of the "dead" particles

$$m_{r,k} \le \delta_d \max_{0 \le s \le k-1} (m_{r,s}) \qquad (4.5)$$

where $m_{r,k}$ is the moving average with the radius r at step k given by

$$m_{r,k} = \frac{\sum\limits_{s=rk}^{r(k+1)-1} d_s}{r} \qquad (4.6)$$

where d_s is the number of "dead" particles at step s and δ_d, the prescribed threshold. In other words the stopping criteria requires that the average death rate drops significantly, relative to the maximum average.

We evaluate the radius of the moving average by

$$r = \left[\gamma \frac{\max(w,h)}{\min(v_{i,j})} + 1 \right], \qquad (4.7)$$

where w, h are the width and the height of the image, γ is a coefficient representing the ratio of the size of the image vs. the size of the tumor, and "[ ]" denotes the nearest integer. The above formula is a conservative estimate of the number of steps required for the majority of the external particles to reach the boundary. For instance, our set of images of 300x300 is characterized by tumors of about $3/4$ of the total area of the image. Since $\min(v_{i,j}) = 1$, $\gamma = \frac{1}{8}$, and $r = 38$. In practice, we considered $r = 25$.

Clearly, in order to optimize the model, we need to stop the particles "not too early" and "not too late". Table 4.3 demonstrates that the proposed stopping criteria tested on 60 US images is applicable, with the best $\delta_d = 0.2$. $\delta_d = 0.1$ is a safe threshold, but the model becomes slightly slower.

Table 4.3 Stopping criteria vs. # of particles

δ_d	#particles/ seed	S (# of iterations)	$\max\limits_{0\leq s\leq S-1}(m_{a,s})$	$m_{a,S}$	Computational time, sec	Classification accuracy (seeds)		
						SEN	SPC	ACC
0.1	3	105	0.424	0.004	1.98	100	97.14	98.18
	5	131	0.616	0.004	2.84	100	97.14	98.18
	10	231	1.381	0.004	6.00	100	97.86	98.64
	50	358	6.818	0.004	27.57	100	97.86	98.64
	100	288	13.600	0.004	34.67	100	97.86	98.64
0.2	3	62	0.424	0.053	1.50	100	97.14	98.18
	5	78	0.616	0.047	1.94	100	97.14	98.18
	10	**173**	**1.381**	**0.025**	**4.97**	**100**	**97.86**	**98.64**
	50	152	6.820	0.672	10.50	100	97.86	98.64
	100	155	13.600	1.379	18.75	100	97.86	98.64
0.4	3	46	0.424	0.134	1.49	100	77.14	92.52
	5	62	0.616	0.085	1.92	100	86.43	93.73
	10	91	1.381	0.186	3.18	100	87.86	94.64
	50	106	6.818	1.421	7.48	100	87.86	94.64
	100	89	13.600	3.579	10.92	100	87.86	94.64

On the other hand, $\delta_d = 0.4$ does not provide the required classification accuracy. For similar collections of the US images, we recommend $\delta_d \in [0.1, 0.2]$ (note that the stopping criterion does not depend on the number of particles). Ten particles per seed seem to be optimal for this collection, in terms of the computational time and accuracy (see Table 4.3). Recall that, the seed classification criterion is given by

$$l_j \leq \Delta_l, \text{ where } l_j = \frac{1}{N_p}\sum_{j=1}^{N_p} l_{i,j} \text{ (see Section 4.2.2) and where } \Delta_l = 0.2S .$$

Finally, Table 4.4 presents a summary of the numerical experiments of 60 US images of breast cancer from 60 different patients obtained by a Philips iU22 ultrasound machine at Thammasat University Hospital. Observe that the experiments have been performed on the US images of breast cancer. Other types of images may require different configurations of the parameters.

46

Table 4.4 Time/accuracy of the ES vs. conventional methods

Model	Initialization time	Correctly Initialized, N_{corr}, %
ES	fast (3-5sec)	excellent (96.7)
TS	very slow (60-90 sec)	excellent (93.3%)
QAI	slow (30-50 sec)	good (86.7)
CoD	very fast (1-2 sec)	very poor (0)
FFS	very fast (1-2 sec)	very poor (0)
PIG	very fast (1-2 sec)	medium (73.3)

Tables 4.5 presents the statistical analysis of the proposed method. The STD of the region-based accuracies is sufficiently small. As far as the contour measures are concerned, more than 70% of the samples lie in the interval [Mean-STD, Mean+STD]. The p-value of the ES is 0.048 which implies that the results are statistically significant.

Table 4.5 The mean and STD of ES model

Statistical Analysis	Average accuracy							
	Contour-based measures				Region-based measures			
	H_1	H_2	H_3	TP	SEN	SPE	ACC	DSC
Mean	7.89	1.80	2.60	93.05	88.69	99.87	97.42	0.989
STD	4.87	0.89	1.77	7.22	4.97	0.14	1.09	0.007

47

4.5 Additional Testing on Public Datasets

We verify whether the proposed model depends on the dataset by testing results obtained on Thammasat University database (Biomed) and several public datasets of the US images. Figure 4.5 shows sample images from Biomed SIIT [7], MedScape [142] and UltrasoundCase.info [143].

(a)   (b)   (c)
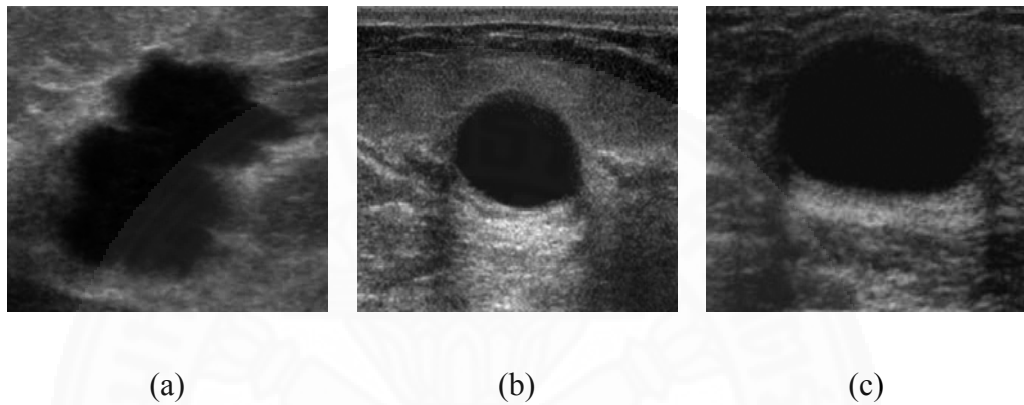
Figure 4.5 Examples of different dataset of US images, a) BioMed SIIT, (b) MedScape, (c) UltrasoundCase.info.

Table 4.6 Accuracy obtained on different datasets (20 images)

Model	Average accuracy							
	Contour-based measures				Region-based measures			
	H_1	H_2	H_3	TP	SEN	SPE	ACC	DSC
ES								
BioMedSIIT	7.89	1.80	2.60	93.05	88.69	99.87	97.42	0.989
MedScape	5.46	1.95	2.57	93.28	90.07	99.61	98.20	0.991
UltrasoundCase.info	6.55	2.05	2.62	93.52	90.15	99.65	99.02	0.992
TS								
BioMedSIIT	8.65	2.15	3.14	89.63	94.45	99.65	98.35	0.989
MedScape	7.54	2.13	3.07	90.58	94.52	99.53	98.45	0.990
UltrasoundCase.info	7.35	2.12	3.06	92.58	94.53	99.54	98.68	0.991

Table 4.6 comparing the results obtained on 20 sample images from each database shows that the accuracy practically does not depend on the particular database.

4.6 Testing Against the Location of Abnormality

We verify whether the proposed model depends on the location of abnormality by changing the location as shown in Figure 4.6 for 20 images from Biomed SIIT database.

(a) Center   (b) Top Left Corner   (c) Bottom Left Corner

(d) Top Right Corner   (e) Bottom Right Corner
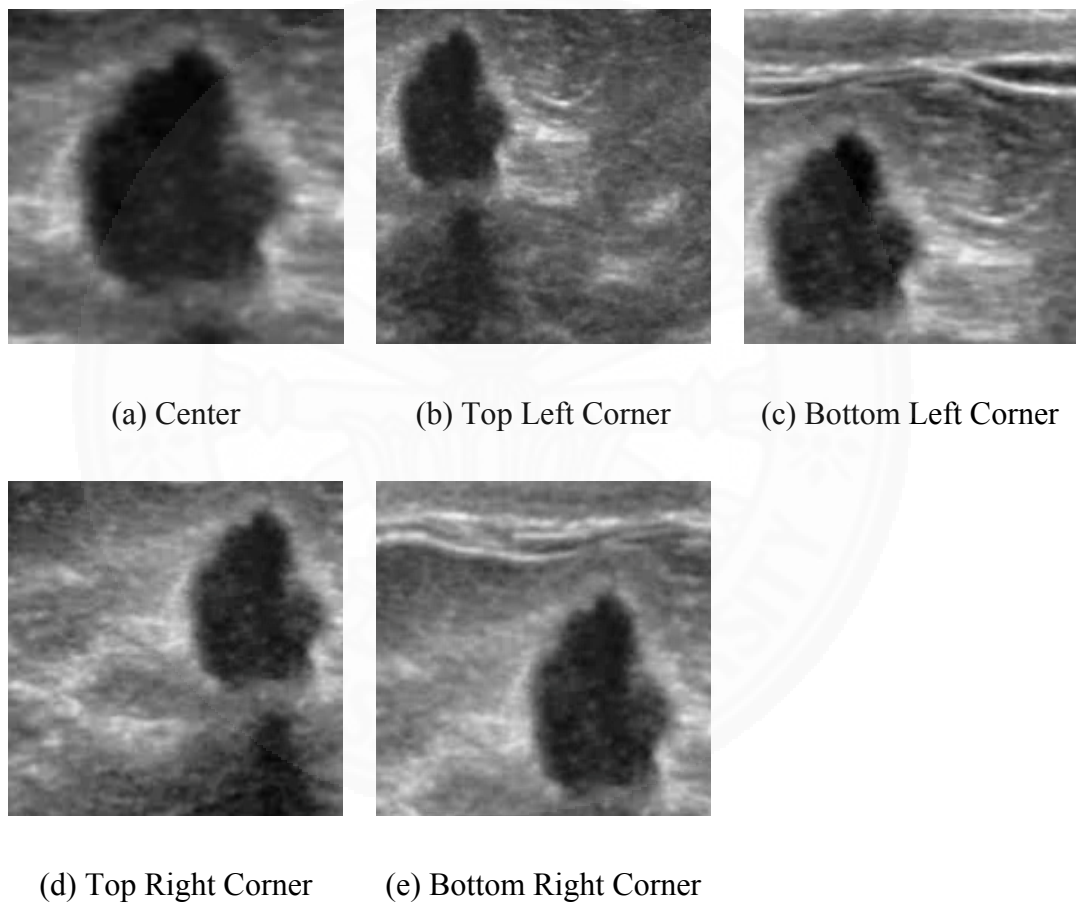
Figure 4.6 Examples of different location of abnormality.

Table 4.7 shows that the results practically do not depend on the location of abnormality.

Table 4.7 Accuracy vs. different tumor location (20 images)

Model	Average accuracy							
	Contour-based measures				Region-based measures			
	H_1	H_2	H_3	TP	SEN	SPE	ACC	DSC
ES								
Center	4.00	1.84	3.74	97.94	92.63	99.99	99.18	0.991
Top Left Corner	4.10	1.93	3.92	97.51	92.39	99.97	99.15	0.990
Bottom Left Corner	4.05	1.88	3.82	97.59	92.63	99.98	99.17	0.991
Top Right Corner	4.00	1.85	3.76	97.84	92.70	99.99	99.19	0.992
Bottom Right Corner	4.24	1.94	3.94	96.83	92.42	99.94	99.16	0.990
TS								
Center	4.10	1.85	3.81	97.62	92.73	99.98	99.17	0.991
Top Left Corner	4.14	1.96	3.99	96.69	92.39	99.97	99.12	0.990
Bottom Left Corner	4.13	1.87	3.81	97.58	92.70	99.98	99.14	0.990
Top Right Corner	4.11	1.90	3.87	97.11	92.63	99.99	99.15	0.991
Bottom Right Corner	4.12	1.95	3.96	97.07	92.30	99.99	99.13	0.990

4.7 Conclusions

The proposed new automatic procedure for initialization of active contours for segmentation of ultrasound images of breast cancer outperforms preceding algorithms. In terms of the accuracy, the ES is better than QAI, CoD, FFS, and PIG, and is comparable with TS. However, the exploding particles are faster than TS. This is because TS may get stuck between the edges or inside the cavities, whereas the exploding particles eventually find their way to the boundary of the image. As far as QAI, CoD, FFS, and PIG are concerned, their weakness is that they are based purely on configurations of the vector field which can be irregular and chaotic. As opposed to that, ES uses the vector field and the edge map at the same time.

50

The method is simple, totally automatic, and does not involve any human intervention. However, it requires several tuning parameters, such as the ratio of the deterministic/random component of the velocity and the coefficients associated with the stopping criteria. These values might depend on the intensity of the noise and the density of the edges. Nevertheless, we conjecture that the proposed values of the parameters, verified on the test US images, are applicable to similar US images without any modifications.

Chapter 5

Conclusions and Recommendations

5.1 Conclusions

The numerical experiments on synthetic and real US images of breast cancer indicate that the proposed procedures work very well to extract tumors from low-contrast US images. The proposed methods combined with the GVF-type snakes are robust and accurate. The two proposed algorithms outperform the following initialization algorithms: QAI, CoD, FFS, PIG and manual initialization. The active contours combined with the proposed initialization outperform Level Set Method [28] and Fuzzy C-mean Clustering [29]. From the testing of noisy low-contrast images of synthetic and real US images of breast cancer, the TS and ES give an excellent result for more than 90% of the images whereas the QAI and PIG solve about 80% and 70% of the cases respectively. In turn the CoD and FFS totally fail. The manual initialization for LSM and FCM can not be compared properly with the automatic initialization, however, even manually selected contours often fail to resolve the tumor. In terms of the computational time, the ES initialization is faster than TS. However, even though the ES is slower than the competing methods, the accuracy of the method is always the highest.

The proposed ES model can be also associated with the artificial life (autonomous multi-agent models) for edge detection. However, all previous models of this type are pixel-based. The agents interact not only with each other but with all neighboring pixels which slows down the computations. Therefore, it is not clear whether the proposed autonomous agents provide an efficient segmentation. Some pixel-based autonomous agents have been proposed characterized by different behaviors such as communication, perception, tagging, reproduction, diffusion, disappearance, etc.

A combination of a multi-agent pixel based model, the proposed ES and a deformable model may probably work even better since the multi-agents will "live" in the pixel based and the edge based environment. However, this is a subject of the further research.

Note that we also can translate this idea into a continuous level (a diffusion model with impenetrable walls). However, the continuous model (parabolic equations) allows the particles (temperature) pass even through the smallest openings in the boundary. As opposed to that, the discrete model defines particles of an appropriate size which may bounce off the boundary even though it has openings. The combination of the small walking particles which are able to penetrate the cavities and large particles which are able to close the boundary (in cooperation with the small particles) may constitute another research direction.

5.2 Limitations

The proposed methods have been designed and implemented for the case of a single object of interest like a malignant or benign tumor. The initialization methods have not been combined with other segmentation methods which also require seeds such as the LSM, clustering, region growing, etc. Furthermore, the model does not work if the contour is characterized by large openings. In this case the inside and outside walking particles with mix together.

5.3 Recommendations

Apart from the multi-agent options mentioned above, possible extensions of the proposed algorithms lie along the lines of combining with the other segmentation methods which require seeds. Further, the method can be improved by involving some secondary features of the object such as the intensity, texture, etc. Finally, the ES can be integrated into the framework of the artificial life as well into artificial intelligence framework (fireflies, ant colony, etc.).

References

1.   Jalalian, A., Mashohor, S.B., Mahmud, H.R., Saripan, M.I., Ramli, A.R., Karasfi, B. (2013). Computer-aided detection/diagnosis of breast cancer in mammography and ultrasound: a review. *Clinical Imaging*, 37 (3), 420-426.

2.   Wissler, R. (2017). *Understanding Medical Radiation.* Retrived January 1, 2017, from https://www.medicalradiation.com/types-of-medical-imaging/imaging-using-x-rays/

3.   Ozdemir, A., Ozdemir, H., Maral, I., Konus, O., Yucel, S., Isik, S. (2001). Differential diagnosis of solid breast lesions: contribution of Doppler studies to mammography and gray scale imaging. *Journal of the American Institute of Ultrasound in Medicine*, 20 (10), 1091-1101.

4.   Cho, N., Jang, M., Lyou, C.Y., Park, J.S., Choi, H.Y., Moon, W.K. (2012). Distinguishing benign from malignant masses at breast US: Combined US elastography and color Doppler US - Influence on radiologist accuracy. *Radiology*, 262 (1), 80-90.

5.   Berg, W.A., Cosgrove, D.O., Doré, C.J., Schäfer, F.K.W., Svensson, W.E., Hooley, R.J., Ohlinger, R., Mendelson, E.B., Balu-Maestro, C., Locatelli, M., Tourasse, C., Cavanaugh, B.C., Juhan, V., Stavros, A.T., Tardivon, A., Gay, J., Henry, J.P., Cohen-Bacrie, C. (2012). Shear-wave elastography improves the specificity of breast US: The BE1 multinational study of 939 masses. *Radiology*, 262 (2), 435-449.

6.   Information Technology Division, National Cancer Institute. (2017). *Hostpital-based cancer registry annual report 2015*. Retrieved May 1, 2017, from http://www.nci.go.th/th/cancer_record/cancer_rec1.html

7.   Biomedical Engineering Research Unit, SIIT. (2015). *Breast cancer images of malignant   solid   mass*.   Retrived   January   1,2015, from http://www.onlinemedicalimages.com/index.php/en/

8.   Kass, M., Witkin, A., Terzopoulos, D. (1988) Snakes: Active contour models. *Computer Vision* 1 (4), 321-331.

54

9.   Rochery, M., Jermyn, I.H., Zerubia, J. (2006). Higher Order Active Contours. *Computer Vision* 69 (1), 27-42.

10.   Xu, C. & Prince, J.L. (1997). Gradient vector flow: a new external force for snakes. *Proceedings of IEEE Society Conference on Computer Vision and Pattern Recognition*, 17-19 June 1997 (pp. 66–71).

11.   Xu, C. & Prince, J.L. (1998). Generalized gradient vector flow external forces for active contours. *Signal Processing*, 71 (2), 131-139.

12.   Nakaguro, Y., Makhanov, S.S., Dailey, M.N. (2011). Numerical Experiments with Cooperating Multiple Quadratic Snakes for Road Extraction. *Geographical Information Science*, 25 (5), 765-783.

13.   Chucherd, S., & Makhanov, S.S. (2011). Sparse phase portrait analysis for preprocessing and segmentation of ultrasound image of breast cancer. *IAENG International Journal of Computer Science*, 38 (2), 146-159.

14.   Liu, Q., Jiang, M., Bai, P., Yang, G. (2016). A novel level set model with automated initialization and controlling parameters for medical image segmentation. *Computerized Medical Imaging and Graphics*, 48, 21-29.

15.   Tauber, C., Batatia, H., Ayache, A. (2010). Quasi-automatic initialization for parametric active contours. *Pattern Recognition Letters*, 31 (1), 83-90.

16.   Hsu, C.Y., Liu, C.Y., Chen, C.M. (2008). Automatic segmentation of liver PET images. *Computerized Medical Imaging and Graphics*, 32 (7), 601-610.

17.   Madabhushi, A., & Metaxas, D.N. (2003). Combining low-, high-level and empirical domain knowledge for automated segmentation of ultrasonic breast lesions. *IEEE Transactions on Medical Imaging*, 22 (2), 155-169.

18.   Doshi, D.J., March, D.E., Crisi, G.M., Coughlin, B.F. (2007). Complex cystic breast masses: diagnostic approach and imaging-pathologic correlation. Radiographics : a review publication of the Radiological Society of North America, 27 (1), 53–64.

19.   Jung, I.S., Thapa, D., Wang, G.N. (2005). Automatic segmentation and diagnosis of breast lesions using morphology method based on ultrasound. In Wang, L., & Jin, Y. (eds.), *Fuzzy Systems and Knowledge Discovery: Proceedings of the Second international conference, FSKD 2005, held in Changsha, China, 27-29*

August, 2005 (pp. 1079-1088). Berlin, Heidelberg,: Part II. Springer Berlin Heidelberg.

20.   Xingfei, G., Jie, T. (2002). An automatic active contour model for multiple objects. *Proceeding of the 16th International Conference on Object recognition supported by user interaction for service robots: Pattern Recognition*, 881-884.

21.   Cohen, I. & Herlin, I. (1995). A motion computation and interpretation framework for oceanographic satellite images. *Proceedings of International Symposium on Computer Vision - ISCV, 21-23 Nov 1995* (13–18).

22.   Cohen, I. & Herlin, I. (1996) Optical flow and phase portrait methods for environmental satellite image sequences. In: Buxton, B. & Cipolla, R. (eds.), *Computer Vision — ECCV '96: Processdings Volume II of the 4th European Conference on Computer Vision, Cambridge, UK, 15–18 April, 1996* (pp. 141-150), Berlin, Heidelberg: Springer Berlin Heidelberg.

23.   Li, J., Yau, W.Y., Wang, H. (2008). Combining singular points and orientation image information for fingerprint classification. *Pattern Recognition* 41 (1), 353–366.

24.   Li, J., Yau, W.Y., Wang, H. (2006). Constrained nonlinear models of fingerprint orientations with prediction. *Pattern Recognition* 39 (1), 102–114.

25.   Shu, C.F. & Jain, R.C. (1994) Vector field analysis for oriented patterns. *IEEE Transactions on Pattern Analalysis and Machine Intelligence* 16 (9), 946–950.

26.   Tian, X., Samarasinghe, S., Murphy, G. (1999). An integrated algorithm for detecting position and size of knots on logs using texture analysis. *Proceedings of the Conference on Image and Visions Computing, University of Canterbury, New Zealand* (pp. 121–132).

27.   Yau, W.Y., Li, J., Wang, H. (2004). Nonlinear phase portrait modeling of fingerprint orientation. *Proceeding of ICARCV 2004 8th Control, Automation, Robotics and Vision Conference, 6-9 Dec. 2004* (pp. 1262-1267).

28.   Li, C., Xu, C., Gui, C., Fox, M.D. (2010). Distance regularized level set evolution and its application to image segmentation. *IEEE Transactions on Image Processing*, 19 (12), 3243-3254.

29.   Li, B.N., Chui, C.K., Chang, S., Ong, S.H. (2011). Integrating spatial fuzzy clustering with level set methods for automated medical image segmentation. *Computers in Biology and Medicine*, 41 (1), 1-10.

30.   Jifeng, N., Chengke, W., Shigang, L., Shuqin, Y. (2007) NGVF: an improved external force field for active contour model. *Pattern Recognition Letters* 28 (1), 58-63.

31.   Guillot, L. & Guyader, C.L. (2009). Extrapolation of vector fields using the infinity Laplacian and with applications to image segmentation. In Tai, X.C., Mørken, K, Lysaker M, Lie K-A (eds.), *Scale Space and Variational Methods in Computer Vision: Proceedings of Second International Conference, SSVM 2009, Voss, Norway, 1-5 June, 2009* (pp. 87-99). Berlin, Heidelberg: Springer Berlin Heidelberg.

32.   Wang, Y., Jia, Y., Liu, L. (2008). Harmonic gradient vector flow external force for snake model. *Electronics Letters*, 44 (2), 105–106.

33.   Li, B. & Acton, S.T. (2007). Active contour external force using vector field convolution for image segmentation. *IEEE transactions on image processing : a publication of the IEEE Signal Processing Society*, 16 (8), 2096-2106.

34.   Cheng, J., Foo, S.W. (2006). Dynamic directional gradient vector flow for snakes. *IEEE transactions on image processing : a publication of the IEEE Signal Processing Society*, 15 (6), 1563-1571.

35.   Wu, Y., Wang, Y., Jia, Y. (2013). Adaptive diffusion flow active contours for image segmentation. *Compututer Vision and Image Understanding*, 117 (10), 1421-1435.

36.   Rodtook, A. & Makhanov, S.S. (2013). Multi-Feature Gradient Vector Flow Snakes for Adaptive Segmentation of the Ultrasound Images of Breast Cancer. *Visual Communication and Image Representation*, 24(8), 1414-1430.

37.   Rangayyan, R.M. & Ayres F.L. (2006). Gabor filters and phase portraits for the detection of architectectural distortion in mammograms. *Medical & Biological & Engineering & Computing*, 44 (10), 883-894.

38.   He, Y., Luo, Y., Hu, D. (2006). Semi-automatic initialization of gradient vector flow snakes. *Electronic Imaging*, 15 (4), 1-8.

39.   Jordan, D. & Smith, P. (2007). *Nonlinear ordinary differential equations: An introduction for scientists and engineers.* 4th ed. Oxford, New York: Oxford University Press.

40.   Chucherd, S., Rodtook, A., Makhanov, S.S. (2010). Phase portrait analysis for multiresolution generalized gradient vector flow. *IEICE Transactions on Information and Systems*, E93.D, 2822-2835.

41.   Jalba, A.C., Wilkinson, M.H.F., Roerdink, J.B.T.M. (2004). CPM: a deformable model for shape recovery and segmentation based on charged particles. *IEEE Transactions on Pattern Analysis and Machine Intelligence*, 26 (10), 1320-1335.

42.   Jalba, A.C., Wilkinson, M.H.F., Roerdink, J.B.T.M. (2004). Automatic image segmentation using a deformable model based on charged particles. In Campilho, A. & Kamel, M. (eds*.), Image Analysis and Recognition: Proceedings of International Conference ICIAR 2004 held in Porto, Portugal, 29 September – 1 October, 2004* (pp. 1-8). Berlin, Heidelberg: Springer Berlin Heidelberg.

43.   Jalba, A.C. & Roerdink, J.B.T.M. (2003). Automatic Segmentation of diatom images. In Petkov, N. & Westenberg, M.A. (eds.), *Computer Analysis of Images an Patterns, Volume 2756 of Lecture Notes in Computer Science: Proceedings of the international Conference, CAIP 2003 held in Groningen, Netherlands, August 2003* (pp. 369-376). Berlin, Heidelberg: Springer Berlin Heidelberg.

44.   Ma, Z., Tavares, J.M.R.S., Jorge, R.M.N. (2009). A review on the current segmentation algorithms for medical images. *Proceedings of the 1st International Conference on Imaging Theory and Applications (IMAGAPP), Portugal*, 135-140.

45.   Noble, J.A. & Boukerroui, D. (2006). Ultrasound image segmentation: a survey. *IEEE Transactions on Medical Imaging*, 25 (8), 987-1010.

46.   Horsch, K., Giger, M.L., Venta, L.A., Vyborny, C.J. (2001). Automatic segmentation of breast lesions on ultrasound. *Medical Physics*, 28 (8), 1652-1659.

47.   Horsch, K., Giger, M.L., Venta, L.A., Vyborny, C.J. (2002). Computerized diagnosis of breast lesions on ultrasound. *Medical Physics*, 29 (2), 157-164.

48.   Horsch, K., Giger, M.L., Vyborny, C.J., Venta, L.A. (2004). Performance of computer-aided diagnosis in the interpretation of lesions on breast sonography. *Acadamic Radioly*, 11 (3), 272-280.

49.   Drukker, K., Giger, M.L., Horsch, K., Kupinski, M.A., Vyborny, C.J, Mendelson, E.B. (2002). Computerized lesion detection on breast ultrasound. *Medical Physics*, 29 (7), 1438-1446.

50.   Drukker, K., Giger, M.L., Vyborny, C.J., Mendelson, E.B. (2004). Computerized detection and classification of cancer on breast ultrasound. *Acadamic Radioly*, 11 (5), 526-535.

51.   Shan, J., Cheng, H.D., Wang, Y. (2012). Completely automated segmentation approach for breast ultrasound images using multiple-domain features. *Ultrasound in Medicine & Biology*, 38 (2), 262-275.

52.   Jiang, P., Peng, J., Zhang, G., Cheng, E., Megalooikonomou, V., Ling, H. (2012). Learning-based automatic breast tumor detection and segmentation in ultrasound images. *The 9th IEEE International Symposium Biomedical Imaging (ISBI), 2-5 May 2012* (pp. 1587–1590).

53.   Jesneck, J.L., Lo, J.Y., Baker, J.A. (2007). Breast mass lesions: computer-aided diagnosis models with mammographic and sonographic descriptors. *Radiology*, 244 (2), 390-398.

54.   Chen, C.M., Chou, Y.H., Han, K.C., Hung, G.S., Tiu, C.M., Chiou, H.J., Chiou, S.Y. (2003). Breast lesions on sonograms: computer-aided diagnosis with nearly setting-independent features and artificial neural networks. *Radiology*, 226 (2), 504-514.

55.   Song, J.H., Venkatesh, S.S., Conant, E.F., Cary, T.W., Arger, P.H., Sehgal, C.M. (2005). Artificial Neural Network to aid differentiation of malignant and benign breast masses by ultrasound imaging. *Proceedings of SPIE, Progress in Biomedical Optics and Imaging 2005*, 148-152.

56.   Joo, S., Yang, Y.S., Moon, W.K., Kim, H.C. (2004). Computer-aided diagnosis of solid breast nodules: use of an artificial neural network based on multiple sonographic features. *IEEE Transactions on Medical Imaging*, 23 (10), 1292-1300.

57.   Huang, Y.L., Wang, K.L., Chen, D.R. (2005). Diagnosis of breast tumors with ultrasonic texture analysis using support vector machines. *Neural Computing & Applications*, 15 (2), 164-169.

58.   Huang, Y.L., Chen, D.R. (2004). Watershed segmentation for breast tumor in 2-D sonography. *Ultrasound in Medical & Biology*, 30 (5), 625-632.

59.   Xiao, G., Brady, M., Noble, J.A., Zhang, Y. (2002). Segmentation of ultrasound B-mode images with intensity inhomogeneity correction. *IEEE Transactions on Medical Imaging,* 21 (1), 48-57.

60.   Boukerroui, D., Baskurt, A., Noble, J.A., Basset, O. (2003). Segmentation of ultrasound images-multiresolution 2D and 3D algorithm based on global and local statistics. *Pattern Recognition Letters*, 24 (45), 779-790.

61.   Kannan, S.R., Devi, R., Ramathilagam, S., Takezawa, K. (2013). Effective FCM noise clustering algorithms in medical images. *Computers in Biology and Medicine*, 43 (2), 73-83.

62.   Son, L.H., Tuan, T.M. (2016). A cooperative semi-supervised fuzzy clustering framework for dental X-ray image segmentation. *Expert Systems with Application*, 46 (C), 380-393.

63.   Zhang, X., Li, X., Feng, Y. (2015). A medical image segmentation algorithm based on bi-directional region growing. *Optik - International Journal for Light and Electron Optics*, 126 (20), 2398-2404.

64.   Chen, D.R., Chang, R.F., Wu, W.J., Moon, W.K., Wu, W.L. (2003). 3-D breast ultrasound segmentation using active contour model. *Ultrasound in Medicine & Biology*, 29 (7), 1017-1026.

65.   Chang, R.F., Wu, W.J., Moon, W.K., Chen, W.M., Lee, W., Chen, D.R. (2003). Segmentation of breast tumor in three-dimensional ultrasound images using three-dimensional discrete active contour model. *Ultrasound in Medicine & Biology*, 29 (11), 1571-1581.

66.   Chang, R.F., Wu, W.J., Tseng, C.C., Chen, D.R., Moon, W.K. (2003). 3-D snake for US in margin evaluation for malignant breast tumor excision using Mammotome. *IEEE Transactions on Information Technology in Biomedicine*, 7 (3), 197-201.

67.   Sahiner, B., Chan, H.P., Roubidoux, M.A., Helvie, M.A., Hadjiiski, L.M., Ramachandran, A., Paramagul, C., LeCarpentier, G.L., Nees, A., Blane, C. (2004). Computerized characterization of breast masses on three-dimensional ultrasound volumes. *Medical Physics*, 31 (4), 744-754.

68.   Chen, D.R., Chang, R.F., Kuo, W.J., Chen, M.C., Huang, Y.L. (2002). Diagnosis of breast tumors with sonographic texture analysis using wavelet transform and neural networks. *Ultrasound in Medicine & Biology*, 28 (10):1301-1310.

69.   Cheng, H.D., Shan, J., Ju, W., Guo, Y., Zhang, L. (2010). Automated breast cancer detection and classification using ultrasound images: A survey. *Pattern Recognition*, 43 (1), 299-317.

70.   James, A.P., Dasarathy, B.V. (2014). Medical image fusion: A survey of the state of the art. *Information Fusion*, 19, 4-19.

71.   Smistad, E., Falch, T.L., Bozorgi, M., Elster, A.C., Lindseth, F. (2015). Medical image segmentation on GPUs – A comprehensive review. *Medical Image Analysis*, 20 (1), 1-18.

72.   Iglesias, J.E., Sabuncu, M.R. (2015). Multi-atlas segmentation of biomedical images: A survey. *Medical Image Analysis*, 24 (1), 205-219.

73.   Ghosh, P., Mitchell, M., Tanyi, J.A., Hung, A.Y. (2016). Incorporating priors for medical image segmentation using a genetic algorithm. *Neurocomputing*, 195, 205-219.

74.   Ma, Z., Jorge, R.N., Tavares, J.M. (2010). A shape guided C-V model to segment the levator ani muscle in axial magnetic resonance images. *Medical Engineering & Physics*, 32 (7), 766-774.

75.   Wang, J., Yeung, S.K., Chan, K.L. (2015). Matching-constrained active contours with affine-invariant shape prior. *Computer Vision and Image Understanding*, 132, 39-55.

76.   Diop, E.H.S., Burdin, V. (2013). Bi-planar image segmentation based on variational geometrical active contours with shape priors. *Medical Image Analysis*, 17 (2), 165-181.

77.   Wang, B., Gao, X., Li, J., Li, X., Tao, D. (2015). A level set method with shape priors by using locality preserving projections. *Neurocomputing*, 170, 188-200.

78.   Li, C. (2006). *Level set for image segmentation*. Matlab File Exchange MathWorks. Retrived January 10, 2016,

from http://www.mathworks.com/matlabcentral/fileexchange/12711-level-set-for-image-segmentation

79.   ABing. (2011). *Spatial Fuzzy Clustering and Level Set Segmentation*. Matlab File Exchange MathWorks. Retrived January 10, 2016,

from http://www.mathworks.com/matlabcentral/fileexchange/31068-spatial-fuzzy-clustering-and-level-set-segmentation. Accessed 10 January 2016

80.   Ma, Z., Tavares, J.M.R.S. (2016). A novel approach to segment skin lesions in dermoscopic images based on a deformable model. *IEEE Journal of Biomedical ans Health Informatics*, 20(2), 615:621.

81.   Ma, Z., Jorge, R.M.N., Mascarenhas, T., Tavares, J.M.R.S. (2013). A level set based algorithm to reconstruct the urinary bladder from multiple views. *Medical Engineering & Physics*, 35(12), 1819-1824.

82.   Ma, Z., Jorge, R.M.N., Mascarenha, T., Tavares, J.M.R.S. (2012). Segmentation of female pelvic cavity in axial T2-weighted MR images towards the 3D reconstruction. *International Journal for Numerical Methods in Biomedical Engineering*, 28, 714–726.

83.   Xie, X., Wu, J., Jing, M. (2013). Fast two-stage segmentation via non-local active contours in multiscale texture feature space. *Pattern Recognition Letters*, 34 (11), 1230-1239.

84.   Krawczyk, B., Schaefer, G. (2014). A hybrid classifier committee for analysing asymmetry features in breast thermograms. *Applied Soft Computing*, 20, 112-118.

85.   Krawczyk, B., Schaefer, G., Woźniak, M. (2015). A hybrid cost-sensitive ensemble for imbalanced breast thermogram classification. *Artificial Intelligence in Medicine*, 65 (3), 219-227.

86.   Krawczyk, B., Filipczuk, P. (2014). Cytological image analysis with firefly nuclei detection and hybrid one-class classification decomposition. *Engineering Applications of Artificial Intelligence*, 31, 126-135.

87.   Filipczuk, P., Krawczyk, B., Woźniak, M. (2013). Classifier ensemble for an effective cytological image analysis. *Pattern Recognition Letters*, 34 (14), 1748-1757.

88.   Krawczyk, B., Galar, M., Jeleń, Ł., Herrera, F. (2016). Evolutionary undersampling boosting for imbalanced classification of breast cancer malignancy. *Applied Soft Computing*, 38, 714-726.

89.   Ji, Z., Xia, Y., Sun, Q., Cao, G., Chen, Q. (2015). Active contours driven by local likelihood image fitting energy for image segmentation. *Information Sciences*, 301, 285-304.

90.   Xu, C., Prince, J.L. (1998). Snakes, shapes, and gradient vector flow. *IEEE Transactions in Image Processing*, 7 (3):359-369.

91.   Tang, J. (2009). A multi-direction GVF snake for the segmentation of skin cancer images. *Pattern Recognition*, 42 (6), 1172-1179.

92.   Wei, M., Zhou, Y., Wan, M. (2004). A fast snake model based on non-linear diffusion for medical image segmentation. *Computerized Medical Imaging and Graphics*, 28 (3), 109-117.

93.   Hsu, C.Y., Chen, S.H., Wang, K.L. (2003). Active contour model with a novel image force field. *Proceeding of the Conference CVGIP-2003, Taiwan*, 477–483.

94.   Li, C., Liu, J., Fox, M.D. (2005). Segmentation of external force field for automatic initialization and splitting of snakes. *Pattern Recognition*, 38 (11), 1947-1960.

95.   Zhu, G., Zhang, S., Zeng, Q., Wang, C. (2010). Gradient vector flow active contours with prior directional information. *Pattern Recognition Letters*, 31 (9), 845-856.

96.   Li, Q., Deng, T., Xie, W. (2016). Active contours driven by divergence of gradient vector flow. *Signal Processing*, 120, 185-199.

97.   Malladi, R., Sethian, J., Vemuri, B. (1995). Shape modeling with front propagation. *IEEE Transactions on Pattern Analysis and Machine Intelligence*, 17 (2), 158–171.

98.   Osher, S., Sethian, J.A. (1988). Fronts propagating with curvature dependent speed: Algorithms based on Hamilton-Jacobi formulation. *Journal of Computational Physics*, 79, 12-49.

99.   Caselles, V., Kimmel, R., Sapiro, G. (1997). Geodesic active contours. *International Journal of Computer Vision*, 22 (1), 61–79.

100.   Siddiqi, K., Lauzie`re, Y.B., Tannenbaum, A., Zucker, S.W. (1998). Area and length minimizing flows for shape segmentation. *IEEE Transactions on Image Processing*, 7 (3), 433–443.

101.   Wang, X., He, L., Wee, W.G. (2004). Deformable contour method: a constrained optimization approach. Internatinal *Journal of Computer Vision*, 59 (1), 87–108.

102.   He, L., Peng, Z., Everding, B., Wang, X., Han, C.Y., Weiss, K.L., Wee, W.G. (2008). A comparative study of deformable contour methods on medical image segmentation. *Image and Vision Computing*, 26, 141–163.

103.   Xu, C., Pham, D., Prince, J. (2000). *Image segmentation using deformable models*. *Handbook of Medical Imaging vol 2: Medical Image Processing and Analysis*, SPIE Press, 129-174.

104.   McInerney, T., Terzopoulos, D. (2000). T-snakes: topology adaptive snakes. *Medical Image Analysis*, 4 (2), 73-91.

105.   Shih, F.Y., Zhang, K. (2007). Locating object contours in complex background using improved snakes. *Computer Vision and Image Understanding*, 105 (2), 93–98.

106.   Mille, J. (2009). Narrow band region-based active contours and surfaces for 2D and 3D segmentation. *Computer Vision and Image Understanding*, 113 (9), 946–965.

107.   Cohen LD, Cohen I (1993) Finite-element methods for active contour models and balloons for 2-D and 3-D images. *IEEE Transactions on Pattern Analysis and Machince Intelligence*, 15 (11), 1131-1147.

108.   Cohen, L.D. (1991). On active contour models and balloons. *CVGIP: Image Understanding*, 53 (2), 211-218.

109.   Zhu, S.C., Yuille, A. (1996). Region competition: unifying snakes, region growing, and Bayes/MDL for multiband image segmentation. *IEEE Transactions on Pattern Analysis and Machine Intelligence*, 18 (9), 884–900.

110.   Shang, Y., Yang, X., Zhu, L., Deklerck, R., Nyssen, E. (2008). Region competition based active contour for medical object extraction. *Computerized Medical Imaging and Graphics*, 32(2), 109–117.

111.   Fenster, S.D., Kender, J.R. (2001). Sectored snakes: evaluating learned energy segmentations. *IEEE Transactions on Pattern Analysis and Machine Intelligence*, 23 (9), 1028–1034.

112.   Fenster, A., Tong, S., Cardinal, H.N., Blake, C., Downey, D.B. (1998). Three-dimensional ultrasound imaging system for prostate cancer diagnosis and treatment. *IEEE Instrumentation & Measurement Magazine*, 1 (4), 32-35.

113.   Jumaat, A.K., Rahman, W.E.Z.W.A., Ibrahim, A., Mahmud, R. (2010). Segmentation of masses from breast ultrasound images using parametric active contour algorithm. *Procedia - Social and Behavioral Sciences*, 8, 640 – 647.

114.   Cvancarova, M., Albresgtsen, F., Brabrand, K., Samset, E. (2005). Segmentation of ultrasound images of liver tumors applying snake algorithms and GVF. *International Congress Series*, 1281, 218-223.

115.   Alemán-Flores, M., Alemán-Flores, P., Álvarez-León, L., Esteban-Sánchez, M.B., Fuentes-Pavón, R., Santana-Montesdeoca, J.M. (2005). Computerized ultrasound characterization of breast tumors. *International Congress Series*, 1281, 1063-1068.

116.   Hamarneh, G., Gustavsson, T. (2000). Combining snakes and active shape models for segmenting the human left ventricle in echocardiographic images. *Computers in Cardiology*, 27,115 –118.

117.   Chen, C.M., Lu, H.H.S., Lin, Y.C. (2000). An early vision-based snake model for ultrasound image segmentation. *Ultrasound in Medicine and Biology*, 26 (2), 273-285.

118.   Mignotte, M., Meunier, J. (2001). A multiscale optimization approach for the dynamic contour-based boundary detection issue. *Computerized Medical Imaging and Graphics*, 25 (3), 265 – 275.

119. Rodtook, A., Makhanov, S.S. (2010). Continuous force field analysis for generalized gradient vector flow field. *Pattern Recognition*, 43 (10), 3522 – 3538.

120. Ma, Z., Tavares, J.M.R.S., Jorge, R.M.N., Mascarenhas, T. (2010). A review of algorithms for medical image segmentation and their applications to the female pelvic cavity. *Computer Methods in Biomechanics and Biomedical Engineering*, 13 (2), 235-246.

121. Ma, Z., Jorge, R.M.N., Mascarenhas, T., Tavares, J.M.R.S. (2011). Novel Approach to Segment the Inner and Outer Boundaries of the Bladder Wall in T2-Weighted Magnetic Resonance Images. *Annals of Biomedical Engineering*, 39 (8), 2287-2297.

122. Ma, Z., Jorge, R.M.N., Mascarenhas, T., Tavares, J.M.R.S. (2013). Segmentation of female pelvic organs in axial magnetic resonance images using coupled geometric deformable models. *Computers in Biology and Medicine*, 43 (4), 248-258.

123. Wang, Y., Liang, J., Jia, Y. (2007). On the critical point of gradient vector flow snake. In: Yagi, Y., Kang, S.B., Kweon, I.S., Zha, H. (eds). *Computer Vision – ACCV 2007: Proceedings of the 8th Asian Conference on Computer Vision held in Tokyo, Japan, 18-22 November 2007* (pp. 754 - 763). Berlin, Heidelberg: Springer Berlin Heidelberg.

124. Ray, N., Acton, S.T. (2003). Merging Parametric Active Contours Within Homogeneous Image Regions for MRI-Based Lung Segmentation. *IEEE Transactions on Medical Imaging*, 22 (2), 189-199.

125. Saha, B.N., Ray, N., Zhang, H. (2009). Snake Validation: A PCA-Based Outlier Detection Method. *IEEE Signal Processing Letters*, 16 (6), 549 – 552.

126. Tauber, C., Batatia, H., Ayache, A. (2005). A general Quasi-automatic initialization for Snakes: application to ultrasound images. IEEE *Internation Conference on Image Processing 2005, 11-14 September 2005*, 806-809.

127. Li, B., Acton, S.T. (2008). Automatic active model initialization via Poisson inverse gradient. *IEEE Transactions on Image Processing*, 17 (8), 1406-1420.

128. Hsua, C.Y., Wang, H.F., Wang, H.C., Tseng, K.K. (2012). Automatic extraction of face contours in images and videos. *Future Generation Computer Systens*, 28 (1), 322–335.

129. Veronese, E., Stramare, R., Campion, A., Raffeiner, B., Beltrame, V., Scagliori, E., Coran, A., Ciprian L., Fiocco U., Grisan, E. (2013). Improved detection of synovial boundaries in ultrasound examination by using a cascade of active-contours. *Medical Engineering & Physics*, 35 (2), 188-194.

130. Selvan, S., Shenbagadevi, S. (2015). Automatic seed point selection in ultrasound echography images of breast using texture features. *Biocybernetics and Biomedical Engineering*, 35 (3), 157-168.

131. Fergani, K., Lui, D., Scharfenberger, C., Wong, A., Clausi, D.A. (2014). Hybrid structural and texture distinctiveness vector field convolution for region segmentation. *Computer Vision and Image Understanding*, 125, 85–96.

132. Liu, S., Peng, Y. (2012). A local region-based Chan–Vese model for image segmentation. *Pattern Recognition,* 45 (7), 2769–2779.

133. Akgul, Y.S., Kambhamettu, C., Stone, M. (1998). Extraction and tracking of the tongue surface from ultrasound image sequences. *Proceedings of IEEE Computer Society Conference on Computer Vision and Pattern Recognition, 23-25 Jun 1998*, 298-303.

134. Ngoi, K.P., Jia, J.C. (1999). An active contour model for colour region extraction in natural scenes. *Image and Vision Computing*, 17 (13), 955-966.

135. Choi, W.P., Lam, K.M., Siu, W.C. (2001). An adaptive active contour model for highly irregular boundaries. *Pattern Recognition*, 34, 323–331.

136. Nakaguro, Y., Dailey, M.N., Marakatat, S., Makhanov, S.S., (2013). Defeating line-noise CAPCHAs with multiple quadratic snakes. *Computer Security*, 37, 91-110.

137. Dubuisson, M.P., Jain, A.K. (1994). A Modified Hausdorff Distance for Object Matching Proceedings. *Proceedings of the 12th International Conference on Pattern Recognition*, 9-13 Oct 1994, 566-568.

138. Fawcett, T. (2006). An introduction to ROC analysis. *Pattern Analysis Letters*, 27, 861-874.

139. Jain, A.K., Zhong, Y., Lakshmanan, S. (1996). Object matching using deformable templates. *IEEE Transactions on Pattern Analysis and Machine Intelligence*, 18 (3), 267-278.

140. Kirimasthong, K., Rodtook, A., Chaumrattanakul, U., Makhanov, S.S. (2017). Phase portrait analysis for automatic initialization of multiple snakes for segmentation of the ultrasound images of breast cancer. *Pattern Analalysis and Application* 20 (1), 239-251.

141. Kirimasthong, K., Rodtook, A., Lohitvisate, W., Makhanov, S.S. (2017). Automatic initialization of active contours in ultrasound images of breast cancer. *Pattern Analysis and Application*, Doi: 10.1007/s10044-017-0627-6, Published online: 7 June 2017.

142. Huff, J.G. (2009). *The Sonographic Findings and Differing Clinical Implications of Simple, Complicated, and Complex Breast Cysts*. MedScape. Retrieved July 10, 2017, from http://www.medscape.org/viewarticle/712949

143. Geertsma, T. (2010). *Palpable mass in the breast*. UntrasoundCase.info. Retrived July 10, 2017, from

http://www.ultrasoundcases.info/Monthly-Case.aspx?month=198&show=1

Appendices

Appendix A
List of Publications

International Journals

1. Kirimasthong, K., Rodtook, A., Chaumrattanakul, U., Makhanov, S.S. (2017). Phase portrait analysis for automatic initialization of multiple snakes for segmentation of the ultrasound images of breast cancer. *Pattern Analysis and Application*, 20 (1), pp. 239-251.

2. Kirimasthong, K., Rodtook, A., Lohitvisate, W., Makhanov, S.S. (2017). Automatic initialization of active contours in ultrasound images of breast cancer. *Pattern Analysis and Application*, Doi: 10.1007/s10044-017-0627-6, Published online: 7 June 2017.

International Conferences

1. Kirimasthong, K., Rodtook, Makhanov, S.S. (2013). Automatic Initialization of Multiple Active Contours Applied to Ultrasound Images of Breast Cancer. *The second Asian Conference on Information Systems (ACIS2013), Phuket, Thailand, 31 October – 2 November, 2013*, pp. 601-604.

2. Kirimasthong, K., Rodtook, Makhanov, S.S. (2014). Automatic Multiple Active Contour Initialization Using Multi-stage Evolution. *The International Conference on Information and Communication Technology for Embedded Systems (ICICTES2014), Ayuthaya, Thailand, 23-25 January, 2014*, pp. 33.